Draft version October 6, 2008
Preprint typeset using LaTeX style emulateapj v. 10/09/06

CHASING HIGHLY OBSCURED QSOS IN THE COSMOS FIELD.

F. Fiore[1], S. Puccetti[2], M. Brusa[3], M. Salvato[4], G. Zamorani[5] T. Aldcroft[6], H. Aussel[7], H. Brunner[3], P. Capak[4], N. Cappelluti[3], F. Civano[6], A. Comastri[5], M. Elvis[6], C. Feruglio[7], A. Finoguenov[3], A. Fruscione[6], R. Gilli[5], G. Hasinger[3], A. Koekemoer[8], J. Kartaltepe[9], O. Ilbert[9], C. Impey[10], E. Le Floc'h[9], S. Lilly[11], V. Mainieri[12], A. Martinez-Sansigre[13], H.J. McCracken[14], N. Menci[1], A. Merloni[3], T. Miyaji[15], D.B. Sanders[9], M. Sargent[13], E. Schinnerer[13], N. Scoville[4], J. Silverman[11], V. Smolcic[14], A. Steffen[4], P. Santini[1], Y. Taniguchi[16], D. Thompson[4,17], J.R. Trump[10], C. Vignali[18], M. Urry[19], L. Yan[4]

Draft version October 6, 2008

ABSTRACT

A large population of heavily obscured, Compton-thick AGN is predicted by AGN synthesis models for the cosmic X-ray background and by the "relic" super-massive black-hole mass function measured from local bulges. However, even the deepest X-ray surveys are inefficient to search for these elusive AGN. Alternative selection criteria, combining mid-infrared with near-infrared and optical photometry, have instead been successful to pin-point a large population of Compton thick AGN. We take advantage of the deep *Chandra* and *Spitzer* coverage of a large area (more than 10 times the area covered by the *Chandra* deep fields, CDFs) in the COSMOS field, to extend the search of highly obscured, Compton-thick active nuclei to higher luminosity. These sources have low surface density and large samples can be provided only through large area surveys, like the COSMOS survey. We analyze the X-ray properties of COSMOS MIPS sources with 24μm fluxes higher than 550μJy. For the MIPS sources not directly detected in the *Chandra* images we produce stacked images in soft and hard X-rays bands. To estimate the fraction of Compton-thick AGN in the MIPS source population we compare the observed stacked count rates and hardness ratios to those predicted by detailed Monte Carlo simulations including both obscured AGN and star-forming galaxies. The volume density of Compton thick QSOs (logL(2-10keV)=44-45 ergs s^{-1}, or logλL_λ(5.8μm)=44.79-46.18 ergs s^{-1} for a typical infrared to X-ray luminosity ratio) evaluated in this way is $(4.8 \pm 1.1) \times 10^{-6}$ Mpc^{-3} in the redshift bin 1.2–2.2. This density is $\sim 44\%$ of that of all X-ray selected QSOs in the same redshift and luminosity bin, and it is consistent with the expectation of most up-to-date AGN synthesis models for the Cosmic X-ray background (Gilli et al. 2007). The density of lower luminosity Compton-thick AGN (logL(2-10keV)=43.5-44) at z=0.7–1.2 is $(3.7 \pm 1.1) \times 10^{-5}$ Mpc^{-3}, corresponding to $\sim 67\%$ of that of X-ray selected AGN. The comparison between the fraction of infrared selected, Compton thick AGN to the X-ray selected, unobscured and moderately obscured AGN at high and low luminosity suggests that Compton-thick AGN follow a luminosity dependence similar to that discovered for Compton-thin AGN, becoming relatively rarer at high luminosities. We estimate that the fraction of AGN (unobscured, moderately obscured and Compton thick) to the total MIPS source population is $49 \pm 10\%$, a value significantly higher than that previously estimated at similar 24μm fluxes. We discuss how our findings can constrain AGN feedback models.

Subject headings: Active Galactic Nuclei

1. INTRODUCTION

Understanding how galaxies formed and how they became the complex systems we observe in the local Universe is a major theoretical and observational effort, mainly pursued using large and deep multi-wavelength surveys. The ubiquitous observation of 'relic' supermassive black holes (SMBH) in the center of nearby bulge

Electronic address: fiore@oa-roma.inaf.it
[1] INAF–Osservatorio Astronomico di Roma, via Frascati 33, Monteporzio (Rm), I00040, Italy
[2] ASI Science data Center, via Galileo Galilei, 00044 Frascati, Italy
[3] Max Planck Institut für extraterrestrische Physik, Giessenbachstrasse 1, D–85748 Garching, Germany
[4] California Institute of Technology, MC 105-24, 1200 East California Boulevard, Pasadena, CA 91125
[5] INAF–Osservatorio Astronomico di Bologna, via Ranzani 1, I–40127 Bologna, Italy
[6] Harvard-Smithsonian Center for Astrophysics, 60 Garden Street, Cambridge, MA 02138
[7] CEA/DSM-CNRS, Universite' Paris Diderot, DAPNIA/SAp, Orme des Merisiers, 91191, Gif-sur-Yvette, France
[8] Space Telescope Science Institute, 3700 SanMartin Drive, Baltimore, MD 21218
[9] Institute for Astronomy, University of Hawaii, 2680 Woodlawn Drive, Honolulu, HI, 96822 USA
[10] Steward Observatory, University of Arizona, Tucson, AZ 85721
[11] Department of Physics, Eidgenossiche Technische Hochschule (ETH), CH-8093 Zurich, Switzerland
[12] European Southern Observatory, Karl-Schwarzschild-str. 2, 85748 Garching bei München, Germany
[13] Max Planck-Institut für Astronomie, Königstuhl 17, D-69117 Heidelberg, Germany
[14] Institut d'Astrophysique de Paris, UMR7095 CNRS, Université Pierre & Marie Curie, 98 bis boulevard Arago, 75014 Paris, France
[15] 1IA-UNAM-Ensenada, Mexico
[16] Department of Physics, Ehime University, 2-5 Bunkyo-cho Matsuyama 790-8577, Japan
[17] Large Binocular Telescope Observatory, University of Arizona, 933 N. Cherry Ave., Tucson, AZ 85721-0065, USA
[18] Universita' di Bologna, via Ranzani 1, Bologna, Italy
[19] Yale Center for Astronomy and Astrophysics, Yale University, P.O. Box 208121, New Haven CT 06520-8121, USA

dominated galaxies, and the discovery of tight correlations between their masses and bulge properties suggest strong links and feedbacks between SMBH, nuclear activity and galaxy evolution (Gebhardt et al. 2000, Ferrarese & Merritt 2000 and references therein). The peak of both nuclear (AGN) and star-formation activities is at $z \gtrsim 1$ (Boyle et al. 1988, Madau et al. 1996, Hopkins et al. 2006, Brandt & Hasinger 2005 and references therein), possibly due to the fact that more gas is available at high-z for both AGN fueling and star-formation. In recent years, a number of evidences have been accumulated showing similar mass-dependent evolution for galaxies and AGN (i.e. black holes). We have robust evidence that massive galaxies are characterized by a star formation history that peaks at $z \gtrsim 2$ (Renzini 1996), while lower mass galaxies are typically younger systems (Cowie et al. 1996). Similarly, the density of the high luminosity AGN (QSO hereinafter, see Table 1 for a quantitative definition) peaks at $z \gtrsim 2$ and declines strongly afterwards, while lower luminosity AGN follow a much smoother behavior, peaking at lower redshifts, z=1-1.5 (Ueda et al. 2003, Cowie et al. 2003, Fiore et al. 2003, Hasinger et al. 2005, La Franca et al. 2005). These trends in the evolution of galaxies and AGN have been dubbed "downsizing" (e.g. Cowie et al. 1996, Franceschini et al. 1999), meaning that large structures tend to have formed earlier and have grown faster than smaller structures. The co-evolution of galaxies and AGN and their downsizing depends on feedback between nuclear and galactic activities (Silk & Rees 1998, Fabian 1999, Granato et al. 2001, 2004, Menci et al 2006, Bower et al. 2006, Daddi et al. 2007). QSOs, presumably hosted in high mass progenitors, must somehow be more efficient at inhibiting star-formation in their host galaxies, by heating the interstellar matter through winds, shocks, and high energy radiation (Silk & Rees 1998, Fabian 1999, Granato et al. 2001, 2004, Di Matteo et al. 2005, Menci et al. 2006, 2008, Bower et al. 2006, Li et al. 2007). In this picture, a short, powerful AGN phase is believed to precede the phase when a galaxy is found in a passive status with red optical and UV colors, most of the star-formation having been inhibited by the AGN activity. Conversely, feedback from less powerful AGN, presumably hosted in low mass progenitors, is more effective in self-regulating accretion and star-formation, and cold gas is left available for both processes for a much longer time. The same cold gas can intercept the line of sight to the nucleus, and therefore a natural expectation of this scenario is that the fraction of obscured AGN to the total AGN population is large at low AGN luminosities and decreases at high luminosities, as it is indeed observed (Lawrence & Elvis 1982, Ueda et al. 2003, Steffen et al. 2003, La Franca et al. 2005, Treister & Urry 2005, 2006, Maiolino et al. 2007, Hasinger 2008, Trump et al. 2008, Della Ceca et al. 2008). Powerful AGN clean their sight-lines more quickly than low luminosity AGN, and therefore the fraction of active objects caught in an obscured phase decreases with the luminosity. Under this hypothesis, the fraction of obscured AGN can be viewed as a measure of the timescale over which the nuclear feedback is at work (Menci et al. 2008). In this respect the trend of the fraction of obscured AGN with the luminosity can be regarded as a manifestation of the AGN downsizing. Obscured AGN are thus laboratories in which to investigate feedback in action.

We call "AGN" objects with their SMBH in an active status. This does not imply that the AGN must dominate the bolometric luminosity, but simply that it is possible to recognize its emission in at least one of the bands of the electromagnetic spectrum. We call "unobscured" those AGN in which the optical and soft X-ray nuclear light is not blocked by gas and dust along the line of sight. AGN in which the nuclear light is blocked or reduced by dust and gas along the line of sight are called "obscured". We further distinguish between moderately obscured AGN (or Compton-thin) and highly obscured AGN (or Compton-thick, CT), see Table 1 for quantitative definitions. While unobscured and moderately obscured AGN can be efficiently selected in current X-ray surveys, even the deepest *Chandra* and *XMM-Newton* surveys detected directly only a handful of CT AGN (e.g. Tozzi et al. 2006, Comastri 2004). However, the SMBH mass function obtained by integrating these X-ray luminosity functions falls short by a factor $\sim 1.5-2$ (depending on the assumed efficiency in the conversion of gravitational energy into radiation) of the SMBH mass function, evaluated by using the $M_{BH}-\sigma_V$ / $M_{BH}-M_B$ relationships and the local bulge's luminosity function (the 'relic' SMBH mass function, Marconi et al., 2004, but also see Merloni & Heinz 2008). AGN synthesis models for the Cosmic X-ray Background (CXB, Treister et al. 2004, Treister & Urry 2005, Gilli et al. 2007) predict a large enough volume density of CT AGN to reconcile the 'active' and 'relic' SMBH mass functions.

Obscured AGN, including CT ones, can be recovered, thanks to the reprocessing of the AGN UV emission in the infrared, by selecting sources with mid-infrared (and/or radio) AGN luminosities but faint near-infrared and optical emission. Houck et al. (2005), Weedman et al. (2006a,b), Yan et al. (2007), Polletta et al. (2008) obtained Spitzer IRS spectra of large samples of relatively bright 24μ sources ($F(24\mu) > 0.7$mJy) with faint optical counterparts, finding that the majority are AGN dominated. The small UV rest frame luminosity implies significant obscuration in these objects. Indeed, Polletta et al. (2006) used X-ray data to infer that some of these infrared bright QSOs are Compton-thick. Martinez-Sansigre et al. (2005, 2007, 2008) obtained optical and Spitzer IRS spectra of sources with $F(24\mu) > 0.3$mJy, and faint optical and near infrared counterpars, finding that most are highly obscured, type 2 QSOs. Brand et al. (2007) obtained infrared spectroscopy of 10 sources with $F(24\mu) > 0.8$mJy and faint optical counterpars, finding that 6 exhibit broad Hα lines. Since both the narrow line region and the UV continuum are strongly extinted, they suggest that the obscuration is due to dust on large scales, withing the host galaxies. Dey et al. (2008) obtained optical spectroscopy of a rather large sample of objects with extreme $F(24\mu m)/F(R)$ flux ratios and $F(24\mu) > 0.3$mJy. They found a redshift distribution centered at $z\sim 2$, implying large luminosities, and concluded that both star-formation and nuclear activity are probably contributing to these luminosities. Finally, Daddi et al. (2007) and Fiore et al. (2008, F08 hereafter) suggested that the majority of the so called 'IR excess' sources in the CDFS, with an extreme $F(24\mu m)/F(R)$ flux ratios and $F(24\mu m)$ as low as 40μJy, are highly ob-

TABLE 1
AGN definitions used in this paper

AGN type	A_V	$\log N_H$ cm^{-2}
Unobscured	$< 5^a$	$\lesssim 22$
Moderately obscured (Compton-thin)	> 5	22–24
Highly obscured (Compton-thick)	$\gtrsim 20^b$	> 24
AGN type	logL(2-10keV) ergs cm^{-2} s^{-1}	$\log N_H$ cm^{-2}
Unobscured QSO	> 44	$\lesssim 22$
Compton-thin QSO	> 44	22–24
Compton-thick QSO	> 44	> 24

[a] From Simpson et al. (1999); [b] Allowing for the fact than obscured AGN and QSO can have gas-to-dust ratios much smaller than the Galactic value, see e.g. Maiolino et al. 2001 and Martinez-Sansigre et al. (2006).

scured, possibly CT AGN at z=1–3. Although Donley et al. (2008) and Pope et al. (2008) disagree with the latter two studies on the AGN fraction at faint 24μm fluxes, it is clear that selecting bright 24μm sources with extreme F(24μm)/F(R) flux ratios may represent a promising method to complement X-ray surveys in obtaining sizable samples of CT AGN and so completing the census of accreting SMBH at these redshifts.

Here we apply and extend this approach to the COSMOS field to estimate the total (unobscured, moderately obscured and CT) AGN fraction to the full MIPS 24μm galaxy population. We take advantage of its deep and uniform coverage at infrared, optical and X-ray wavelengths, to select and validate samples of CT AGN at z=0.7–2. The COSMOS sample contains sources which have IR/optical properties similar to those in the *Chandra* Deep Fields (CDFs) but are ~ 10 times brighter, and are therefore much more luminous than the CDFs AGN at the same redshift. Our goal is to select a sizable sample of high luminosity CT QSOs to measure accurately their volume density and to understand whether their obscuration properties are similar to those of lower luminosity AGN. This will allow us to understand whether the correlation between the fraction of obscured AGN and luminosity holds for CT QSOs, and to extend this study up to z$\sim$ 2. Such luminous sources are rare, and only taking advantage of the large area covered by COSMOS they can be found in significant number to make statistical studies. The total area covered by COSMOS is 2 deg^2 but in this work we limit the analysis to the area covered by deep Chandra observations (~ 0.9 deg^2, $\gtrsim 10$ times the area in CDFs).

The paper is organized as follows: Section 2 presents the datasets used in this work and the selection of the CT QSO sample from the *Spitzer* MIPS 24μm COSMOS sample; Section 3 discusses the X-ray properties of the MIPS selected sources; Section 4 presents the result of fitting the broad band spectral energy distributions (SEDs) of the MIPS selected sources with galaxy and AGN templates; Section 5 presents our evaluation of the infrared selected CT QSO volume density and finally Section 6 gives our conclusions. A $H_0 = 70$ km s^{-1} Mpc^{-1}, Ω_M=0.3, $\Omega_\Lambda = 0.7$ cosmology is adopted throughout.

2. DATASETS AND SAMPLE SELECTION

The Cosmic Evolution Survey (COSMOS) field (Scoville et al. 2007) is a so far unique area for its deep & wide comprehensive multiwavelength coverage, from the optical band with *Hubble* and ground based 8m class telescopes, to infrared with *Spitzer*, to X-rays with *XMM-Newton* and *Chandra*, to the radio with the VLA. The COSMOS field samples a volume at high redshift ($z \lesssim 2$) which is ~ 15% of that sampled by SDSS at z$\lesssim$0.15.

For this work we use the *Spitzer* MIPS 24μm COSMOS catalog derived from Cycle 2 shallow observations (Sanders et al. 2007). We do not use in this work the cycle 2 deep MIPS test area because it covers only a small fraction of the *Chandra*-COSMOS area. The cycle 2 catalog has been cleaned of spurious sources (mostly asteroids) by comparison with the much deeper MIPS mosaic obtained in Cycle 3 (Aussel et al. 2008, a reliable catalog from this mosaic is in preparation and will be used in a follow-up publication). We consider only MIPS 24μm sources with a signal to noise ratio > 4, implying a 24μm flux limit of $\sim 550\mu$Jy. We limit the analysis to the area covered by *Chandra* observations (~ 0.9 deg^2, centered on RA=10 00 20 dec=+02 09 28, Elvis et al. 2008). The sample includes 919 sources, and we refer in the following to this sample as the COSMOS Bright MIPS Sample, see Table 2 for further detail.

The *Spitzer* MIPS catalog has been cross correlated with the IRAC catalog [20] (Sanders et al. 2007) the optical multi-band catalog (Capak et al. 2007) and the K band catalog (McCracken et al. 2008). IRAC, K-band and optical counterparts of the MIPS sources have been carefully identified with a 2 step approach: first, each MIPS source has been associated with the most likely IRAC counterpart within 2 arcsec from the MIPS centroid, then IRAC positions have been correlated with the optical and K-band catalogs with a matching radius of 0.5 arcsec. 859 sources of the COSMOS bright MIPS catalog have counterparts in all IRAC, optical and K bands, 53 sources have counterparts in only one or two catalogs. Finally, 4 sources have optical counterpart too close to a bright sources (and therefore no reliable photometry is available) while for the remaining 3 sources no optical counterpart was assigned (they are either residual asteroids or too faint to be detected).

The X-ray properties of the MIPS selected sources have been studied using the *Chandra* data. Chandra observed the COSMOS field for a total of 1.8 Msec. The survey uses a series of 36 heavily overlapped ACIS-I 50 ksec pointings to give an unprecedented uniform effective exposure of 185 ksec over a large area. Particular care was taken in performing accurate astrometric corrections and in the reduction of the internal background (see Elvis et al. 2008 for details). The residual background is very stable over the full field at $\lesssim 2$ counts/200 ksec over an area of 2 arcsec radius, comparable with the *Chandra* beam size, see Table 2 for further details. Uniform coverage and low background make the *Chandra* COSMOS (C-COSMOS) dataset ideal for stacking analyses.

2.1. *Redshifts*

For 96 % of the COSMOS bright MIPS sample either spectroscopic or robust photometric redshifts have been obtained. Accurate spectroscopic redshifts are present for 394 MIPS sources, 43% of the sample (Lilly et al.

[20] http://irsa.ipac.caltech.edu/cgi-bin/Gator/nph-scansubmit=Select&projshort=COSMOS

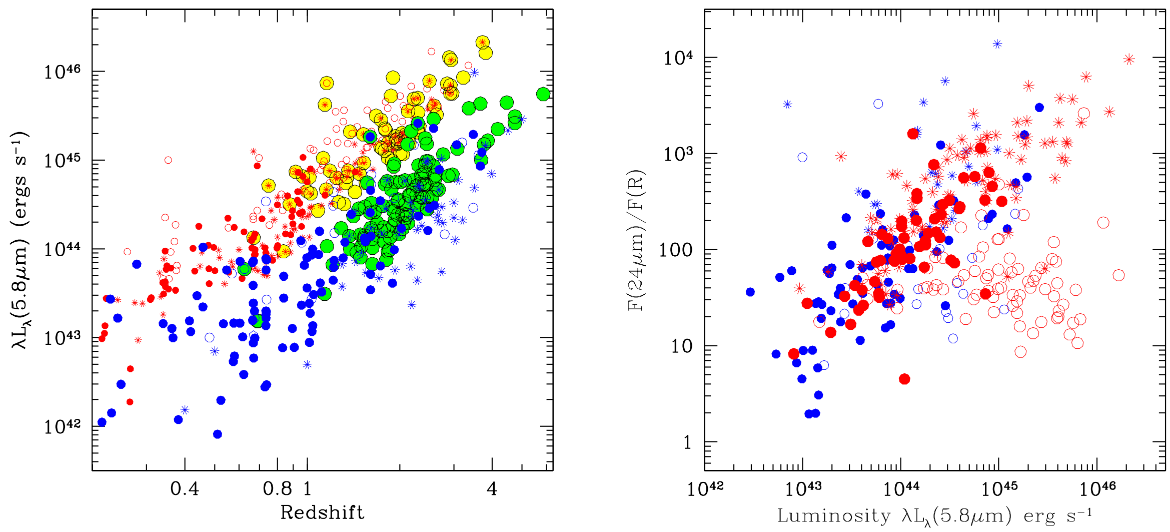

Fig. 1.— [Left panel:] The redshift-infrared luminosity, $\log(\lambda L_\lambda(5.8\mu m))$, plane for the C-COSMOS sources (red and yellow points) and the CDF-S sources (blue and green points). Red and blue circles are sources directly detected in the X-rays. Yellow and green points are 24μm, non X-ray detected sources with $F(24\mu\mathrm{m})/F(R) > 1000$ and $R - K > 4.5$. [Right panel:] F(24μm)/F(R) as a function of the 5.8μm luminosity for two X-ray source samples (GOODS-MUSIC, blue symbols, C-COSMOS, red symbols). In both panels open circles correspond to spectroscopic type 1 AGN, filled circles to non type 1 AGN and asterisks to objects with photometric redshifts. Note that F(24μm)/F(R) of non broad line AGN is strongly correlated with the luminosity at 5.8μm.

TABLE 2
Main datasets used in this paper

Dataset	Area	Total exposure	Typical exposure	FWHM	Detected sources	Flux limit
C-COSMOS	0.9deg^2	1.8Msec	90-185ksec^b	$2''^c$	1760	2×10^{-16} ^{d}
S-COSMOS (MIPS)	0.9deg^2	58.2hr	80sec	$5''^e$	919	550μJy

[a] Typical exposure; [b] ~half of the total area is covered with an effective exposure of ~ 185ksec, the remaining half has an effective exposure of ~ 90ksec; [c] average for four overlapping fields; [d] ergs cm^{-2} s^{-1} 0.5-2 keV; [e] PSF core.

2007, Trump et al. 2007,2008).

Regarding photometric redshifts, we used both the computation of Ilbert et al. (2008) and of Salvato et al. (2008), which made use of about 30 photometric data points (including 12 intermediate filters observed with SUBARU). The first concentrates on objects with I(AB)< 26.5, with SEDs dominated by the integrated stellar population at $\lambda < 5.5\mu$m. The achieved accuracy for the MIPS selected sample is $\sigma(\Delta z/(1+z)) = 0.01$ for I< 24. The accuracy degrades at I> 24 ($\sigma(\Delta z/(1+z)) = 0.05$). The second photometric redshift catalog deals with the XMM-COSMOS (Hasinger et al. 2007) sources that are dominated by AGN emission. For better results i) correction for variability, ii) luminosity priors for point-like sources, and iii) a new set of SED templates have been adopted. Thus, for the first time an accuracy comparable to those of photometric redshift for non-active galaxies has been achieved ($\sigma(\Delta z/(1+z)) < 0.02$ and less that 5% outliers). This second photometric dataset, as specific for X-ray detected sources, was used when the MIPS selected source was associated to an *XMM-Newton* detection. The median redshift of the COSMOS bright MIPS sample is 0.64 with interquartile 0.36. 230 sources have z> 1 and 56 z> 2. Tables 3 and 4 also give the median redshift and its interquatile of MIPS samples selected in intervals of F(24μm)/F(R) and R-K color, see next section.

2.2. *Optical, near infrared and mid infrared color selection*

F08 proposed a criterion, based on high mid-infrared to optical flux ratios and red optical colors, to efficiently select candidate CT AGN, and applied this method to the CDF-S area. Briefly, they selected a sample of candidate CT AGN by using the combination of F(24μm)/F(R)> 1000 and R-K> 4.5 colors. They demonstrated that the selected sample was indeed mainly made by CT AGN through a stacking analysis of the *Chandra* X-ray data. The CDF-S infrared selected, CT AGN have z~1–3, and $\lambda L_\lambda(5.8\mu m) \approx 10^{44-45}$ ergs s^{-1}, corresponding to intrinsic X-ray (2-10 keV) luminosities $\approx 10^{43-44}$ ergs s^{-1}. F08 limited their analysis to MIPS sources with F(24μm)/F(R)> 1000 and R-K> 4.5, a minority of the full MIPS source population. For this reason they did not compute AGN volume densities nor AGN fractions with respect to the full CDFS MIPS galaxy sample. Here we apply the F08 method to the C-COSMOS field and extend their analysis to the full MIPS source population. This allows us to compute proper AGN volume densities and AGN fractions with respect to the full MIPS source population.

Fig. 1 (left panel) compares the 5.8μm luminosities and redshifts of the CDF-S (green) and C-COSMOS (yellow) MIPS selected sources not directly detected in X-rays and with F(24μm)/F(R)> 1000 and R-K> 4.5, to those of the X-ray detected population (red and blue symbols for the C-COSMOS and CDF-S fields respec-

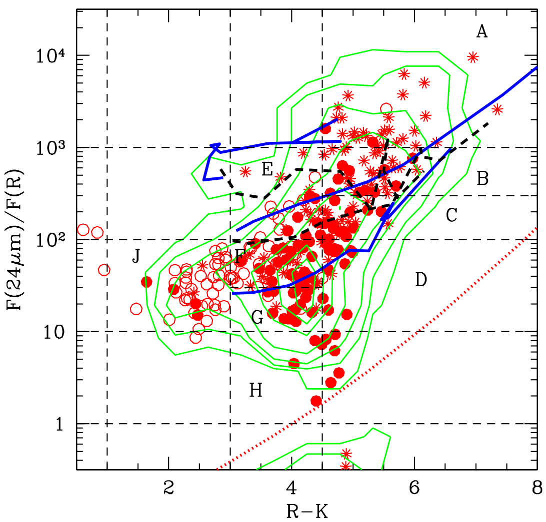

FIG. 2.— F(24μm)/F(R) as a function of R-K color for the X-ray detected population with a luminosity $> 10^{38}$ ergs s^{-1}. Open circles = type 1 AGN; filled circles = non type 1 AGN; asterisks = photometric redshifts. Iso-density contours of all COSMOS 24μm sources are overlaid to the plot. Expected evolution from z= 0 to z=5 for three obscured AGN (blue continuous lines), two star-burst (black dashed lines) and a passive elliptical galaxy (red dotted line) are shown for reference (see F08 for details on the SEDs used). The nine cells defined in the F(24μm)/F(R) plane for the stacking analysis are labeled with letters from A to J (see Section 2.2 for details).

tively). Monochromatic luminosities were computed using a linear interpolation between the observed 8μm and 24μm fluxes at the wavelength corresponding to 5.8μm at the source rest frame.

Both MIPS selected and X-ray selected COSMOS sources have luminosities $\sim$ 10 times higher than the CDF-S sources at the same redshifts, as expected since luminous QSOs are rarer than low luminosity AGN and the C-COSMOS survey covers an area about 10 times larger than the CDF-S at a 10 times brighter 24μm flux limit ($\sim$ 550μJy and 40μJy for C-COSMOS and CDFS respectively).

Fig. 1 (right panel) shows F(24μm)/F(R) as a function of the 5.8μm rest frame luminosity λL_λ(5.8μm), for the C-COSMOS and CDF-S X-ray sources. Unobscured AGN (open symbols in Fig. 1) have F(24μm)/F(R) in the range 10-200, uncorrelated with λL_λ(5.8μm), as expected because the nuclear emission dominates both optical and mid infrared wavelengths. Obscured AGN (filled symbols) have F(24μm)/F(R) spanning a broader range, and correlated with λL_λ(5.8μm). For a flux limited sample the luminosity is strongly correlated with the redshift (Fig. 1 left panel). Therefore, sources with high F(24μm)/F(R) (and high 5.8μm luminosity) have also redshift systematically higher than sources with lower F(24μm)/F(R).

Fig. 2 shows the distribution of F(24μm)/F(R) as a function of the R-K color. F(24μm)/F(R) of X-ray selected, obscured AGN is correlated with the R-K color, as found by F08 for the CDF-S X-ray sources. The isodensity contours of the 24μm selected sources (green curves) follow roughly the same correlation. Unlike the 24μm selected GOODS-MUSIC sources, we do not find a bimodal distribution in R-K colors for the COSMOS sources at high F(24μm)/F(R) values (see Fig. 3, right panel in F08). This is probably due to the higher COSMOS flux limits. The faint, blue, star-forming galaxies found in the GOOD-MUSIC sample are not common in the COSMOS Bright MIPS sample.

CT AGN can also have values of the F(24μm)/F(R) and R-K colors smaller than those adopted by F08, although their fraction to the full infrared selected population is probably small. To properly account for these sources we extend the F08 approach, by analyzing the full F(24μm)/F(R) – R-K diagram. We divided this plane in nine cells (see Fig. 2). The boundaries of the cells were chosen according to the following criteria: 1) cover most of the F(24μm)/F(R) – R-K plane; 2) sample regions not to big in this plane; 3) but at the same time regions containing a number of sources big enough to be statistically meaningful. These nine cells contain most of the COSMOS Bright MIPS sample (87%). Our goal is to estimate the fraction of CT AGN to the total MIPS source population in each of these cells. Table 3 and 4 give the number of MIPS selected sources in each cell, along with the median redshift and luminosity (with their interquartile ranges) of both MIPS sources with (Table 3) and without (Table 4) a direct X-ray detection.

3. X-RAY PROPERTIES OF THE 24μM SELECTED SOURCES

3.1. *Sources with a direct X-ray detection*

232 sources of the COSMOS Bright MIPS sample are present in the C-COSMOS and XMM-COSMOS catalogs (Elvis et al. 2008, Civano et al. 2008, Brusa et al. 2007, 2008a). In addition to these sources we also consider as "detections" 47 sources with more than 10 background-subtracted *Chandra* counts in the full 0.5-7 keV band, within 5 arcsec of the position of the MIPS source but not present in the C-COSMOS and XMM-COSMOS catalogs. This allows us to identify: 1) faint X-ray sources (given the average background, 10 background-subtracted counts in a 5 arcsec radius area corresponds to a probability $\sim 5\times10^{-3}$ that the detected counts are due to a background fluctuation); 2) MIPS sources with a nearby X-ray source; and 3) MIPS sources found in X-ray groups and clusters of galaxies. The total number of MIPS sources with an X-ray counterpart is 279 ($\sim$ 30% of the full MIPS sample, 254 sources in the nine cells defined in Fig. 2). 11 sources do not have K band detections, while the remaining 14 sources are scattered in the diagram outside the considered cells (R-K<1 and F(24μm)/F(R)< 10). Table 3 gives the fraction of MIPS sources with a direct *Chandra* and/or *XMM-Newton* detection in the 9 F(24μm)/F(R) and R-K cells. The fraction of MIPS sources with a direct X-ray detection is minimum ($\sim$ 13%) in cell G, while it is maximum (79%) in cell J. Most of the X-ray sources in the latter cell have been spectroscopically identified (95%) and the majority turned out to be type 1 QSOs (90%), as expected from their colors.

Table 3 gives the median and interquartile range of the X-ray and infrared luminosities of the MIPS sources with X-ray detection in the 9 cells. The X-ray luminosity is computed in the rest frame 2-10 keV band to ease the comparison with previous studies. It is computed from the observed 0.5-7 keV flux, assuming a power law spectrum $F(E) \propto E^{-alpha_E}$ with energy index $\alpha_E = 0.8$

TABLE 3
MIPS sources with a direct *Chandra* detection

Cell	F(24μm)/F(R)	R-K	# of MIPS sources	# of X-ray det.	$< z >$	$< logL(5.8\mu m) >$ ergs s^{-1}	<logL(2-10keV)> ergs s^{-1}	<(H-S)/(H+S)>[a]
A	> 1000	> 4.5	73	31 (40%)	1.55±0.53	45.20±0.44	43.51±0.40	0.50± 0.34
B	$300 - 1000$	> 4.5	98	34 (35%)	0.96±0.13	44.58±0.27	43.15±0.41	0.44±0.31
C	$100 - 300$	> 4.5	105	24 (23%)	0.73±0.12	44.12±0.19	42.69±0.57	0.58±0.22
D	$10 - 100$	> 4.5	65	14 (22%)	0.50±0.25	43.80±0.20	42.01±0.65	0.48±0.28
E	$100 - 1000$	$3 - 4.5$	72	26 (36%)	0.90±0.37	44.61±0.46	43.17±0.78	0.29±0.31
F	$30 - 100$	$3 - 4.5$	187	61 (33%)	0.48±0.21	43.94±0.35	42.60±0.87	0.00±0.22
G	$10 - 30$	$3 - 4.5$	144	19 (13%)	0.17±0.07	43.29±0.26	40.85±0.85	0.28±0.41
H	$1 - 10$	$3 - 4.5$	14	4 (29%)	0.13±0.18	43.16±0.68	41.00±0.74	0.35±0.22
J	$10 - 100$	$1 - 3$	52	41 (79%)	1.48±0.33	45.30±0.32	44.15±0.34	-0.06±0.12

[a] H=1.5-6 keV, S=0.3-1.5 keV.

TABLE 4
MIPS sources without a direct *Chandra* detection

Cell	F(24μm)/F(R)	R-K	# of MIPS sources	$< z >$	$< logL(5.8\mu m) >$ ergs s^{-1}	Counts 1.5-6keV	Counts 0.3-1.5keV	<(H-S)/(H+S)>[a]	CT AGN fraction
A	> 1000	> 4.5	42	1.90±0.40	45.24 0.24	58.9±8.5	18.0±4.7	0.53±0.14	$0.94^{+0.06}_{-0.08}$
B	$300 - 1000$	> 4.5	64	1.01±0.31	44.37 0.40	54.1±8.1	30.4±6.1	0.28±0.12	$0.72^{+0.14}_{-0.19}$
C	$100 - 300$	> 4.5	81	0.79±0.14	44.01 0.17	42.2±7.2	36.9±6.7	0.07±0.12	$0.51^{+0.17}_{-0.18}$
D	$10 - 100$	> 4.5	51	0.37±0.12	43.76 0.24	31.7±6.2	31.1±6.2	0.01±0.14	$0.42^{+0.16}_{-0.23}$
E	$100 - 1000$	$3 - 4.5$	46	0.70±0.22	44.06 0.43	27.7±5.8	36.1±6.6	-0.13±0.14	$0.26^{+0.29}_{-0.26}$
F	$30 - 100$	$3 - 4.5$	126	0.37±0.11	43.61 0.16	91.6±10.6	112.6±11.7	-0.10±0.08	$0.31^{+0.19}_{-0.16}$
G	$10 - 30$	$3 - 4.5$	125	0.23±0.06	43.30 0.21	54.8±8.2	108.9±11.5	-0.33±0.09	< 0.40
H	$1 - 10$	$3 - 4.5$	10	0.11±0.04	42.57 0.29	1.3±1.3	10.4±3.6	$-0.78^{+0.41}_{-0.22}$	< 0.20
J	$10 - 100$	$1 - 3$	11	0.34±0.12	43.52 0.35	0.8±1.0	17.7±4.6	$-0.92^{+0.35}_{-0.08}$	< 0.05

[a] H=1.5-6 keV, S=0.3-1.5 keV.

and Galactic N_H. It is not corrected for absorption, and therefore it should be considered a lower limit to the intrinsic luminosity. The log ratio between the observed 5.8μm and 2-10 keV median luminosities of the 35 type 1 AGN in cell J is 1.15. This can be considered to be little affected by absorption and therefore representative of the ratio between the intrinsic AGN luminosities. The highest luminosity log ratio is for the objects in bin A. Its value (1.7) is significantly higher than in bin J, thus suggesting some obscuration or intrinsically low X-ray emission in the X-ray counterparts of the MIPS sources in this cell.

Table 3 also gives the median and interquartile of the hardness ratios (H-S)/(H+S) computed using the source counts detected in the 0.3-1.5 keV (S) and 1.5-6 keV (H) bands. The hardness ratio expected for a power law spectrum with $\alpha_E = 0.8$ and no absorption in addition to the Galactic one is -0.1. Values between 0.2 and 0.8 imply absorbing column densities between 10^{22} and 10^{23} cm^{-2} (i.e. Compton-thin absorbers) at typical redshifts of 1-2. Note that the hardness ratio of X-ray sources with R-K>4.5 is systematically higher than that of bluer sources. Similar results were found by Mignoli et al. (2004), Brusa et al. (2005) and Mainieri et al. (2007). Indeed, the sample of R-K>4.5 sources is dominated by narrow line AGN (only 1 broad line AGN out of 43 objects with narrow line or absorption line optical spectra, 30 of which with logL(2-10keV)> 42 ergs s^{-1}, and therefore likely to host an active nucleus). Converely, 69 of the 122 objects with R-K<4.5 and logL(2-10keV)> 42 ergs s^{-1} are broad line AGN.

3.2. *X-ray stacking analysis of the sources without a direct X-ray detection*

The total number of COSMOS bright MIPS sources without a direct X-ray detection is 640. Twenty-three sources are bright stars while 610 sources have either a spectroscopic or a photometric redshift (224 and 386, respectively). Finally, seven sources are either strongly blended (4) or too faint in any optical band; in both cases the photometry is poor and unreliable and photometric redshift are not available. Table 4 gives the number of sources without a direct X-ray detection in each of the 9 F(24μm)/F(R) and R-K cells along with their median infrared luminosities and interquartile ranges. The median redshifts and 5.8μm luminosities of the MIPS sources without a direct X-ray detection in all cells but J are similar to those with X-ray detection. This suggests that most if not all QSOs in cell J have been detected in X-rays, and that the remaining sources are inactive galaxies or very faint AGN.

To gain information on the X-ray properties of the MIPS sources without a direct X-ray detection we performed a detailed stacking analysis of the *Chandra* counts at the position of all MIPS source for the samples in the 9 F(24μm)/F(R) and R-K cells. Indeed, the *Chandra* deep and uniform coverage allows us to increase the sensitivity (by factors of $\times 10 - 100$) using the stacking technique (Daddi et al. 2007, Steffen et al. 2007, F08). Stacking analysis was performed using both the web-based tool for stacking analysis of *Chandra* data prepared by T. Miyaji (http://saturn.phys.cmu.edu/cstack/) and software developed at ASDC by S. Puccetti. Results from the two software in the standard bands 0.5-2 keV and 2-8 keV were fully consistent for all 9 samples. Stacking was performed on single ACIS-I exposures and on the combined mosaic. The results were again fully consistent.

Errors on stacked net source counts and count rates are computed by using both Poisson statistics and a "bootstrap" method (by resampling the objects in the input source list). 500 bootstrapped stacked count rate are generated for each source list. Poisson errors turned out to be smaller than the bootstrap error by 3-5%. In the following analysis we conservatively increase the Poisson error by 10% to account for other possible systematic errors.

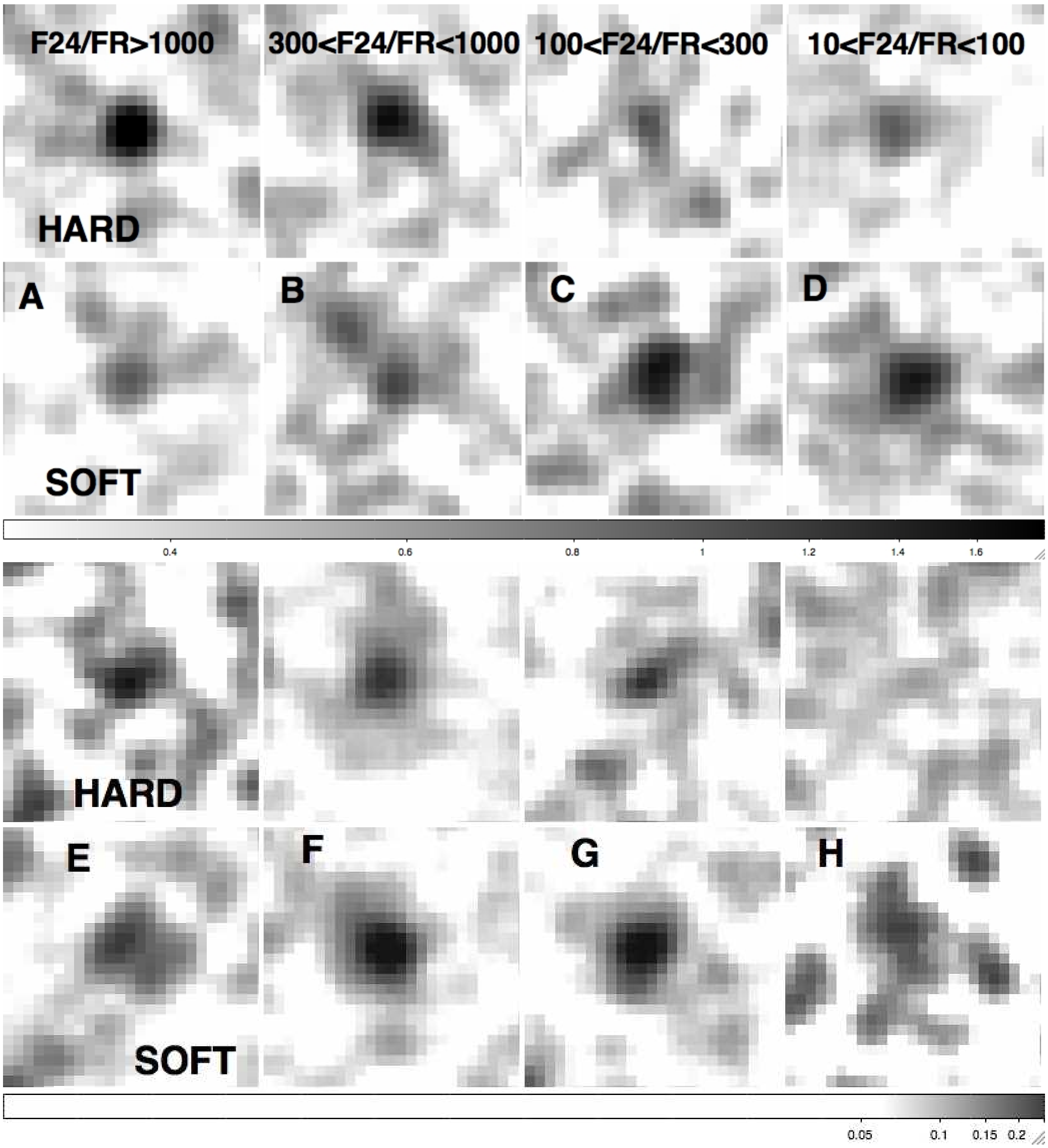

Fig. 3.— Stacked *Chandra* images in the hard 1.5-6 keV and soft 0.3-1.5 keV bands of COSMOS MIPS sources not directly detected in X-rays in eight $F(24\mu m)/F(R)$ cells (A,B,C,D,E,F,G,H). Images have sides of 12 arcsec and have been smoothed with a gaussian with 1.5 arcsec σ.

Stacking was performed in two energy band, to allow the evaluation of a hardness ratio. The signal to noise at high X-ray energies is limited by the internal background, whose spectrum is nearly constant as a function of the energy. Indeed the 2-8 keV band has an internal background ~ 4 times higher than the 0.5-2 keV band. To optimize the analysis at high energies we performed the stacking in several different energy bands and chose the band which gives the highest signal to noise ratio for most of the nine samples. The 1.5-6 keV band gave the best results in terms of signal to noise. In the following we present hardness ratio computed by using this band and the 0.3-1.5 keV band. We performed similar analysis using the 1.5-4 keV and 1.5-5 keV bands as the higher energy band obtaining always qualitatively similar results.

Source extraction regions were also chosen to optimize the signal to noise ratio. We adopted a box with 5 arcsec side (100 ACIS-I square pixels area). A slightly lower signal to noise ratio is obtained using boxes with 3 and 6 arcsec side.

Stacked counts in both energy bands are given in Table 4. Detections with a signal to noise higher than 4 are obtained in all cells but cells H and J. Fig. 3 shows the stacked images of the sources in all cell but J and in the two energy bands, while Table 4 and Fig. 4 shows the hardness ratio (H-S)/(H+S) derived from the stacking analysis as a function of F(24μm)/F(R) for the 9 cells. The samples with the highest $F(24\mu m)$/F(R) and red colors (cells A and B) also have the hardest X-ray hardness ratios. A common concern in stacking analyses is that the results may not be representative of population properties, if they are biased by one or a few sources in the stack. We detect in the stack of the sources in cells A and B 59 and 54 background subtracted counts in the 1.5-6 keV band, respectively. Sources can enter in the stack only if they give less than 10 counts in a region of 5 arcsec radius around the MIPS position in the full 0.5-7 keV band. Sources with an higher number of counts are excluded. Given this threshold the stacked counts in cells A and B must be produced by at least 6 sources, and probably by many more, since it would be highly unlikely to have 6 sources near the chosen threshold and all the rest with zero counts.

The hardness ratios of the stacks of the sources without a direct X-ray detection in cells A and B are similar to the median hardness ratios of the X-ray detected sources in the same cells (Table 3). Taken at face values, these hardness ratios can be explained by a power law spectra with energy index ~ -0.5 and ~ 0 respectively, reduced at low energy by Galactic absorption only. Since neither AGN or known star-forming galaxies have such hard emission spectrum, the observed hardness ratio strongly suggest significant rest frame obscuration. However, for the stacked samples it is not easy to convert a hardness ratio in a typical column density. A direct conversion could produce contradictory results because the X-ray spectrum of the MIPS sources is likely to be more complex than a simple obscured power law. For example, a scattering component can dominate the soft X-ray counts. Furthermore, samples corresponding to different cells have different average redshifts, and therefore comparing hardness ratios is not straightforward, as they are biased towards measuring 'softer' HRs for an obscured AGN at high redshift. To investigate further these issues we performed detailed Monte Carlo simulations as described in the following section.

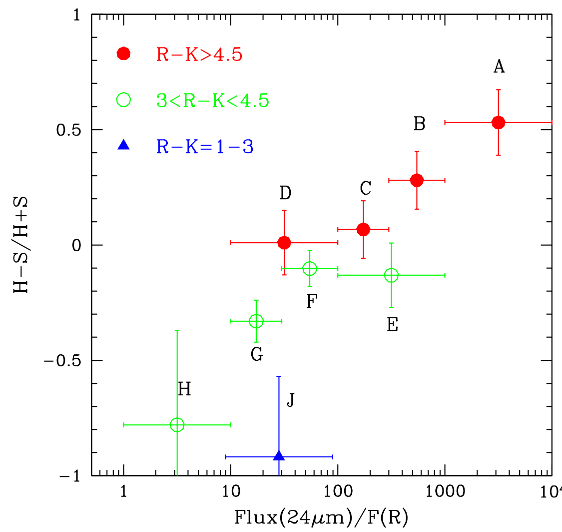

FIG. 4.— Average hardness ratio (H-S)/(H+S) as a function of F(24μm)/F(R) for the sources without direct X-ray detection. Filled circle = cells A, B, C , D; open circles = cells E, F, G, H; filled triangle = cell J.

3.3. *Simulations to assess the fraction of obscured AGN in the 24μm source samples*

Following F08, we used the observed flux in the stacked images, together with the hardness ratio H-S/H+S, to constrain the fraction of CT AGN in the MIPS samples. For the MIPS sources in each of the 9 F(24μm)/F(R) and R-K cells we generated simulated X-ray count rates and hardness ratios as a function of the fraction of obscured AGN to the total MIPS source population in each cell, assuming that the sources without an X-ray detection are either obscured AGN or star-forming galaxies. We started from the observed redshift and infrared luminosities. For the AGN we assumed the log(λL_{λ}(5.8μm)/L(2-10 keV)) luminosity ratio given by the following relationship to obtain unobscured 2-10 keV luminosities:

$$logL(2-10keV) = 43.574 + 0.72(logL(5.8\mu m) - 44.2)$$

$$if\ logL(5.8\mu m) > 43.04 \qquad 1$$

$$logL(2-10keV) = logL(5.8\mu m) - 0.3$$

$$if\ logL(5.8\mu m) < 43.04$$

This has been calibrated using the Type 1 AGN in the CDF-S (Brusa et al. 2008b) and C-COSMOS (Civano et al. 2008) fields as shown in Fig. 5. The derived relation assumes that the 2-10 keV luminosity, computed directly from the observed fluxes without any correction for intervening absorption, can be considered representative of the intrinsic X-ray luminosity. This is a good approximation for most of the points. However, seven outliers (one in the CDFS sample and six in the C-COSMOS sample), show a low X-ray luminosity, given their infrared luminosity, suggestive of significant X-ray obscuration in these sources. These seven points were therefore excluded from the analysis. The logL(2-10keV)–log(λL_λ(5.8μm) linear regression coefficient in eq. 1 turns out to be very similar to that found by Steffen et al. (2006, 0.643). The relationship in eq. 1 is consistent with the log(λL_λ(5.8μm)/L(2-10 keV)) luminosity ratio of the highly obscured AGN in F08, and Silva et al. (2004). In particular, it is well consistent with the ratio found for the type 2 QSO IRAS09104+4109 (Piconcelli et al. 2007, 2008). For the star-forming galaxies we assumed a log(λL_λ(5.8μm)/L(2-10 keV)) luminosity ratio of 2.38 with a gaussian dispersion of 0.2 (see Ranalli et al. 2003).

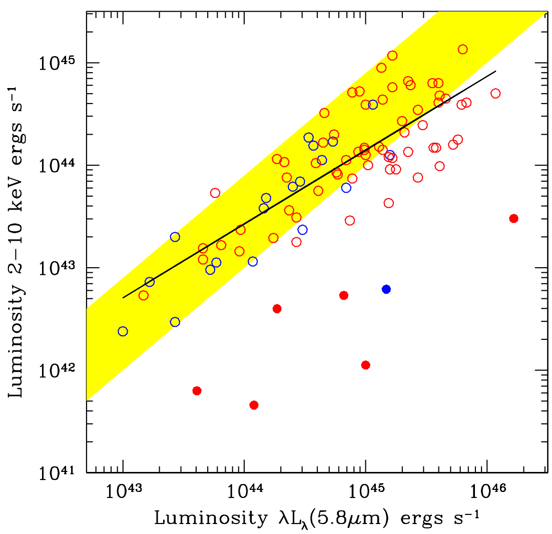

Fig. 5.— The 2-10 keV luminosity (not corrected for obscuration) as a function of the 5.8μm luminosity for 2 samples of type 1 AGN: C-COSMOS (red symbols) and CDF-S (blue symbols). For most of the points this 2-10 keV luminosity can be considered representative of the intrinsic X-ray luminosity. Filled circles identify seven outliers with small X-ray luminosity with respect to their infrared luminosity, suggesting X-ray absorption in these sources, and therefore that the intrinsic X-ray luminosity is likely underestimated in these cases. For this reason these sources have been excluded from the analysis. The black solid line is the best fit linear regression in eq.1. The shaded region is the linear extrapolation of the intrinsic X-ray-to-mid-infrared luminosity ratio found in the local Universe (Lutz et al. 2004).

We assumed that the star-forming galaxies are not obscured in X-rays, while the AGN are highly obscured. We used the Gilli et al. (2007) N_H distribution. This distribution is rapidly increasing towards high column densities, it peaks at about $10^{23.5}$ and then slowly decreases in the Compton-thick regime. The shape is obtained by requiring a simultaneous fit of both the X-ray background spectrum and the source counts in different energy bands (0.5-2 keV , 2-10 keV and 5-10 keV). We chose randomly an N_H from the Gilli et al. distribution for each MIPS source. For column densities $\gtrsim 3 \times 10^{24}$ cm^{-2} we assumed that the direct emission is completely blocked by photoelectric absorption and Compton scattering. We used power law spectra with an energy index equal to 0.8 for the AGN and 0.9 for the star-forming galaxies. In both cases we assumed a gaussian dispersion with $\sigma = 0.2$ (Ranalli et al. 2003). For the AGN we also assumed a Compton reflection component with the same normalization and energy index of the power law component, assuming an inclination of the reflecting material to the line of sight of 60 degrees, and a scattering component with the same spectral index of the power law component and normalization 1/100 of that of the power law component. This is a conservative value which accounts for recent results on highly obscured AGN with very small low energy scattering component (Ueda et al. 2007, Comastri et al. 2007). Fluxes in the 0.3-1.5 keV and 1.5-6 keV band were computed by using the unobscured 2-10 keV luminosities and the assumed spectrum. Finally, count rates were computed by using the Chandra on axis response.

We run 12 series of simulations (12 different realizations for each of the sources in each of the 9 cells), varying the fraction of AGN between 0 and 100% of the MIPS sources in each cell. This fraction is then evaluated in each cell by comparing the output of the simulation with the results of the stacking analysis. Since this analysis was performed excluding the sources directly detected in X-rays, also simulations providing more than 10 counts in the 0.3–6 keV band were excluded from the analysis. Most ($>95\%$) of the simulated AGN with column densities $\lesssim 10^{24}$ cm^{-2} turned out to have more than 10 counts in the 0.3-6 keV band, and were excluded from the analysis. This confirms that most unobscured and Compton-thin AGN would have been detected directly by *Chandra*. On the other hand, simulations with $N_H > 10^{24}$ cm^{-2} produced more than 10 counts $\sim 10-20\%$ of the times in cells A and B. This suggests that some of our faint Chandra detections might be Compton-thick AGN.

Using these simulations we converted the observed hardness ratios in a fraction of obscured, most of them CT, AGN to the total MIPS source population in each of the 9 cells. Fig. 6 left panel shows the calibration plot for cell A as an example. Fig. 6 right panel shows the derived fraction of obscured AGN to the total MIPS source population as a function of F(24μm)/F(R). These fractions are also given in Table 4. At the end of the procedure we verified that the number of sources excluded in each cell is roughly similar to the number of sources actually detected in the real images.

We studied how the derived fractions vary by changing some of the assumptions made to build the simulations. The results turned out qualitatively similar to those reported in Fig. 6 and Table 4 in all cases. We first studied the impact on the results of a higher count threshold to exclude entries from the simulations. Setting the threshold at 20 counts rather than 10 does not change the fraction of obscured AGN in cells A and B, while it slightly reduces this fraction in the other cells.

Assuming a flat N_H distribution with a cut-off at $N_H = 10^{26}$ cm^{-2} instead of the Gilli et al. (2007) distribution decreases slightly the predicted hardness ratios, thus increasing the fractions of obscured AGN by 5-10%. The reason is that this flat distribution has a fraction of objects in the logN_H bin 25-26 higher than the Gilli et al. distribution.

Assuming a fixed conversion factor between the infrared and X-ray luminosities equal to that given by eq. 1 at logL(2-10keV)=44 (6.3) does not change significantly the predicted hardness ratios. Assuming a fixed factor twice the previous feature, as if additional components in addition to the nuclear one contribute significantly to the 5.8μm luminosity, increases slighlty the predicted hardness ratios, decreasing the fraction of obscured AGN needed to reproduce the observed ratios by $\sim 5\%$.

The main parameter affecting the predicted hardness ratio, in addition to the fraction of highly obscured AGN, is the energy index assumed for the star-forming galaxies. Assuming a 20% steeper (or flatter) spectral index for these objects increases (or decreases) the fractions of obscured AGN by $\sim 10\%$. The hardest hardness ratios are observer in cells A and B. These ratios can be produced by a power law spectrum with energy index -0.5 and 0 respectively reduced at low energy by Galactic absorption only. Should star-forming galaxies at z$\sim$ 1.9 and ~ 1 (the median redshift of the sources in cells A and B respectively), exhibit such extremely hard spectra, they will be able to explain the observed hardness ratios.

4. SED FITTINGS

To characterize the infrared SED of the MIPS selected sources we fitted the SED with a library of empirical templates (Polletta et al. 2007, Pozzi et al. 2007, F08, Salvato et al. 2008), fixing the redshift to the spectroscopic redshift or, if this is not available, to the photometric redshift. To limit the importance of dust extinction we limited the analysis to the observed bands with wavelengths $\gtrsim 2\mu$m. We used the 25 templates of F08 plus additional templates of hybrid galaxy plus AGN sources by Salvato et al. (2008). Table 5 and 6 give the number of sources best fitted by four broad template categories, in each of the nine cells for sources with and without a direct X-ray detection. We counted as obscured AGN sources best fitted by the Salvato et al. (2008) hybrid models with an AGN contribution larger than 50%. Sources best fitted by hybrid templates with a smaller AGN contribution are counted as passive or star-forming galaxies. Note that the hybrid models of Salvato et al. (2008) are normalized around 1μm, and therefore templates with an AGN contribution $>$ than 50% at this wavelength may still have the bolometric luminosity domininated by starlight. We see that most sources in cell A of both samples are best fitted by obscured AGN templates (81% and 75% respectively).

Concerning the sample with a direct X-ray detection, the fraction of obscured or unobscured AGN to the total MIPS source population is dominant in all cells but G and D, where the majority of best fit templates are those of star-forming galaxies. Unobscured AGN templates are numerous in cell J, consistently with the spectroscopic identification of the X-ray sources in this cell (83% of the identified sources are type 1 AGN).

Conversely, the number of best fit unobscured AGN templates among the samples of MIPS sources without a direct X-ray detection is small in all cells, as expected, since these objects would be more easily directly detected in X-rays. The fraction of best fit, obscured AGN templates to the total is high in cells A and C, while the number of best fit, star-forming galaxies templates is high in cells D, F and especially in cell G, where the totality of best fit templates are those of star-forming galaxies (Table 6).

In conclusion, the result of the SED fitting is qualitatively consistent with the results obtained from the analysis of the X-ray properties of the MIPS sources presented in the previous sections and summarized in Fig. 6.

5. THE AGN FRACTION

We can now evaluate the total AGN fraction (including unobscured, moderately obscured and highly obscured AGN) in a 24μm source sample. About 75% of the MIPS sources with a direct Chandra detection have an X-ray (2-10 keV) luminosity $> 10^{42}$ ergs $^{-1}$, and are therefore likely to host an AGN. This already makes $\sim 23\%$ of the full COSMOS MIPS sample. Taken at face values, the infrared selected, CT AGN fractions given in Table 4 would imply that $36\pm11\%$ of the COSMOS MIPS sources without a direct Chandra detection host an AGN ($\sim 26\%$ of the full MIPS sample) a fraction similar to that of the X-ray detected AGN. The total fraction of AGN in the full MIPS sample, obtained by adding the two previous fractions, is $49 \pm 10\%$. At the typical 24μm fluxes of the COSMOS bright MIPS sample (flux limit $\sim 550\mu$Jy, median flux $\sim 750\mu$Jy) this is quite a large fraction, compared with previous studies (see Brand et al. 2006 and references therein). A more accurate comparison with the study of Brand et al. (2006) can be made by considering the sources at z$>$ 0.6 only (Brand et al. use this redshift cut to avoid contamination from low-z star-forming galaxies). The left panel of Fig. 7 shows the AGN fractions in the COSMOS MIPS bright sample at z$>$ 0.6 for both sources with a direct X-ray detection and CT AGN, selected using infrared/optical colors and the *Chandra* stacking analysis presented in Sections 3.2 and 3.3. The fraction of MIPS AGN with a direct X-ray detection is already higher than the Brand et al. (2006) estimates at the same 24μm fluxes. The fraction of AGN with X-ray luminosity higher than 10^{43} ergs s^{-1} is consistent with the Brand et al. estimates. The fraction of X-ray AGN is also of the same order of magnitude of that of CT AGN. Adding the fractions of X-ray selected and CT AGN results in a total fraction of AGN in the COSMOS bright MIPS sample at z$>$ 0.6 of 0.67 ± 0.06, a factor of 2 higher than the Brand et al. (2006) estimates. The reason for this apparent inconsistency is that while Brand et al. (2006) assume that the AGN dominates the bolometric luminosity, in many of the sources of our MIPS sample the AGN the bolometric luminosity is dominated by the host galaxy. This can be also appreciated by considering the right panel of Fig. 7. It shows the distribution of the F(24μm)/F(8μm) flux ratio for several COSMOS MIPS samples at z$>$ 0.6. X-ray selected, type 1 AGN peak around log(F(24μm)/F(8μm))=0, and their distribution is consistent with that of X-ray detected AGN in the Bootes field. On the other hand, the distribution of X-ray selected AGN with an optical spectrum not showing broad lines (non type 1 AGN), and that of X-ray AGN with only a photometric redshift, are significantly shifted toward higher log(F(24μm)/F(8μm) values. Note as the latter distribution is similar to the distribution of sources in Cell A without a direct X-ray detection. Brand et al. (2006) associate to the AGN population the peak of the MIPS source distribution around log(F(24μm)/F(8μm)=0 and therefore miss part of the X-ray selected AGN without broad lines in their optical spectra or without optical spectra, and CT

TABLE 5
Template fits to the infrared SEDs of MIPS sources with a direct X-ray detection

Template	A	B	C	D	E	F	G	H	J
Passive galaxies[a]	0	0	0	0	0	1	0	1	0
Star-forming galaxies[b]	0	3	2	9	6	15	18	3	1
Obscured AGN and QSOs[c]	25	20	21	5	15	33	1	0	19
Unobscured AGN and QSOs[d]	6	9	1	0	5	12	0	0	19
Total	31	33	24	14	26	61	19	4	41

[a]Elliptical + S0 + hybrid passive with AGN contribution < 50%; [b]Spiral + M82 + Arp220 + N6090 + hybrid with AGN contribution < 50%; [c]Seyfert 1.8 + Seyfert 2 + red QSOs + I19254 + Mark231 + A2690_75 + BPM16274_69 + IRAS09104+4109 + NGC6240 + hybrid passive and active with AGN contribution ≥ 50%; [d] Seyfert 1 + QSOs.

TABLE 6
Template fits to the infrared SEDs of MIPS sources without a direct X-ray detection

Template	A	B	C	D	E	F	G	H	J
Passive galaxies[a]	0	0	0	0	0	1	0	0	0
Star-forming galaxies[b]	9	31	16	42	19	65	125	10	1
Obscured AGN and QSOs[c]	30	28	63	8	25	59	0	0	9
Unobscured AGN and QSOs[d]	3	3	0	0	2	0	1	0	1
Total	40	64	81	51	46	125	125	10	11

[a]Elliptical + S0 + hybrid passive with AGN contribution < 50%; [b]Spiral + M82 + Arp220 + N6090 + hybrid with AGN contribution < 50%; [c]Seyfert 1.8 + Seyfert 2 + red QSOs + I19254 + Mark231 + A2690_75 + BPM16274_69 + IRAS09104+4109 + NGC6240 + hybrid passive and active with AGN contribution ≥ 50%; [d] Seyfert 1 + QSOs.

AGN without a direct X-ray detection with a higher log(F(24μm)/F(8μm) ratio. Both populations could be recovered in the COSMOS field thanks to the much deeper X-ray coverage (a *Chandra* exposure time 20-40 times longer than that on the BOOTES field), which allowed the direct detection of Seyfert 2 like galaxies up to z∼ 1 and a detailed stacking analysis of the MIPS sources without a direct X-ray detection.

6. THE DENSITY OF CT AGN

In the previous Sections we estimated the fraction of obscured AGN to the total MIPS source population, not detected directly in X-rays, but visible in the stacked *Chandra* images, in each of the 9 cells defined in the F(24μm)/F(R) – R-K diagram. Our simulations showed that most of these AGN are likely to be CT and therefore we will call them CT AGN (or CT QSOs when referring to high luminosity sources) for the sake of simplicity. We can now compute the volume density of the MIPS selected sources, correcting for this fraction, to obtain the density of CT AGN in different redshift and luminosity bins. We use for this calculation the standard 1/V$_{max}$ method (Schmidt 1968, Lilly et al. 1995, Cowie et al. 2003). While it is well known that this method is not free from biases (the main one is that it does not account for evolution within each L and z bin), it is robust enough to derive general trends (see e.g. Cowie et al. 2003).

Fig. 8 left panel shows the infrared luminosity - redshift plane for the MIPS sources without a direct X-ray detection in cells A, B and C. The loci of four SEDs of highly obscured AGN computed at the 24μm flux limit of 550μJy are also showed. Two redshift-luminosity bins chosen for the computation of the CT AGN volume density are also marked in figure. The two bins have been chosen according to the following three criteria:

TABLE 7
Number of sources in luminosity-redshift bins

Redshift	log(λL_λ(5.8μm))	Cell	# of sources
1.2 – 2.2	44.79-46.18	A	21 (40)
1.2 – 2.2	44.79-46.18	B	15 (64)
1.2 – 2.2	44.79-46.18	C	2 (81)
1.2 – 2.2	44.79-46.18	D	0 (51)
1.2 – 2.2	44.79-46.18	E+F+G+H	3 (306)
0.7 – 1.2	44.06-44.79	A	2 (40)
0.7 – 1.2	44.06-44.79	B	25 (64)
0.7 – 1.2	44.06-44.79	C	29 (81)
0.7 – 1.2	44.06-44.79	D	2 (51)
0.7 – 1.2	44.06-44.79	E+F+G+H	11 (306)

1. The bins must lie above the lowest limit for an obscured AGN SED corresponding to our 24μm flux limit. We can therefore considered the source samples in these bins relatively little affected by complex selection effects.

2. The redshift and luminosity ranges should not be too large, to avoid strong biases in the calculation of the volume densities, see above.

3. The bins should be cut to maximize the number of sources included in the analysis at the relevant redshifts, to keep statistical errors small.

Fig. 8, left panel, shows that a reasonable compromise is to limit the analysis to the sources in the redshift-luminosity bins given in Table 7. This table gives for each of these bins the number of MIPS sources without a direct X-ray detection in some of the nine F(24μm)/F(R) and R-K cells (the total number of sources in each cell is given in brackets in the last column of Table 7).

Because of the strong correlation of F(24μm)/F(R) (and therefore R-K) with log(λL_λ(5.8μm)) the largest numbers of sources with large infrared luminosity are found in cells A and B, which are also the cells with the highest fraction of CT AGN. On the other hand, the largest number of sources with intermediate luminosity at z=0.7–1.2 are found in cell C. The contribution of sources in cells E,F,G and H is small in both luminosity-

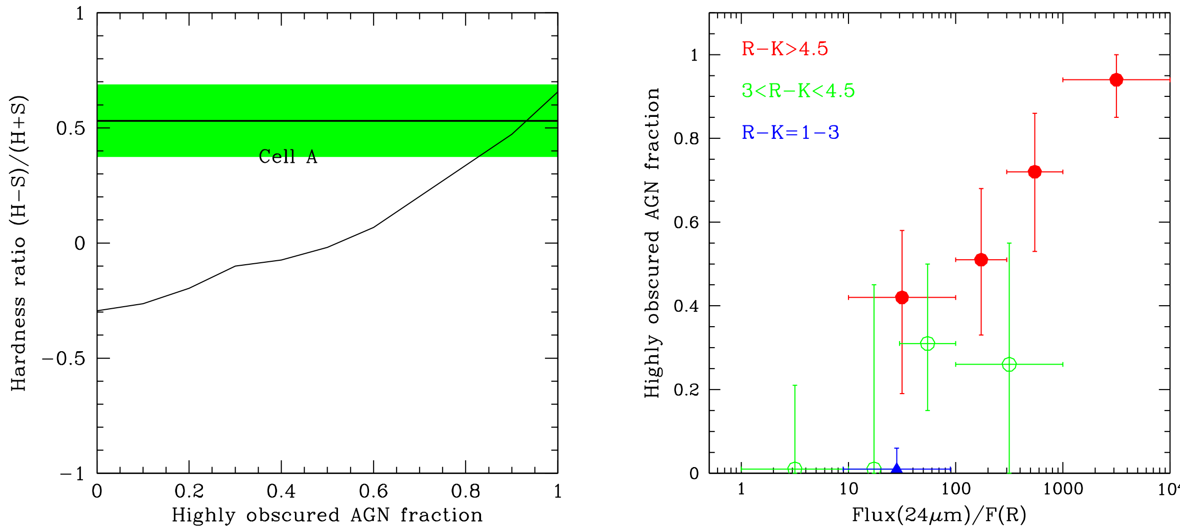

FIG. 6.— [Left panel:] the hardness ratio (H-S)/(H+S) as a function of the fraction of CT AGN in the sample of MIPS sources with a spectroscopic or photometric redshift in cell A. The solid curve is the result of Monte Carlo simulations (see text for details); the thick horizontal lines is the average hardness ratios measured in cell A. The colored bands mark the hardness ratio statistical uncertainties.[Right panel:] The fraction of CT AGN to the total MIPS source population as a function of F(24μm)/F(R). Filled circle = cells A, B, C , D; open circles = cells E, F, G, H; filled triangle = cell J.

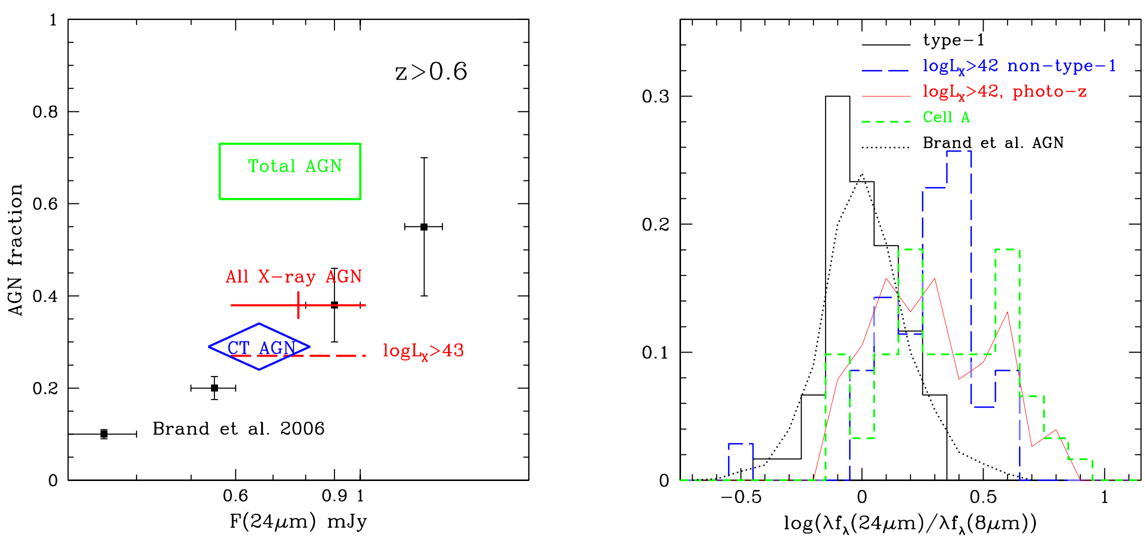

FIG. 7.— [Left panel:] The AGN fraction as a function of the 24μm flux for z> 0.6 sources. Red cross and dashed line = AGN with a direct X-ray detection; blue diamond = CT AGN without a direct X-ray detection; green box = total AGN fraction. The black points are the AGN fraction of Brand et al. (2006) [Right panel:] The distribution of the F(24μm)/F(8μm) flux ratio for several COSMOS MIPS samples at z> 0.6: black, solid histogram = type 1 AGN with a direct X-ray detection; blue, long-dashed histogram = type 2 AGN with a direct X-ray detection; red thin solid line = sources with photometric redshift and an X-ray luminosity > 10^{42} ergs s^{-1}; green, short-dashed histogram = sources in Cell A without a direct X-ray detection. The Brand et al. (2006) X-Bootes AGN distribution is showed as a comparison (black, dotted line).

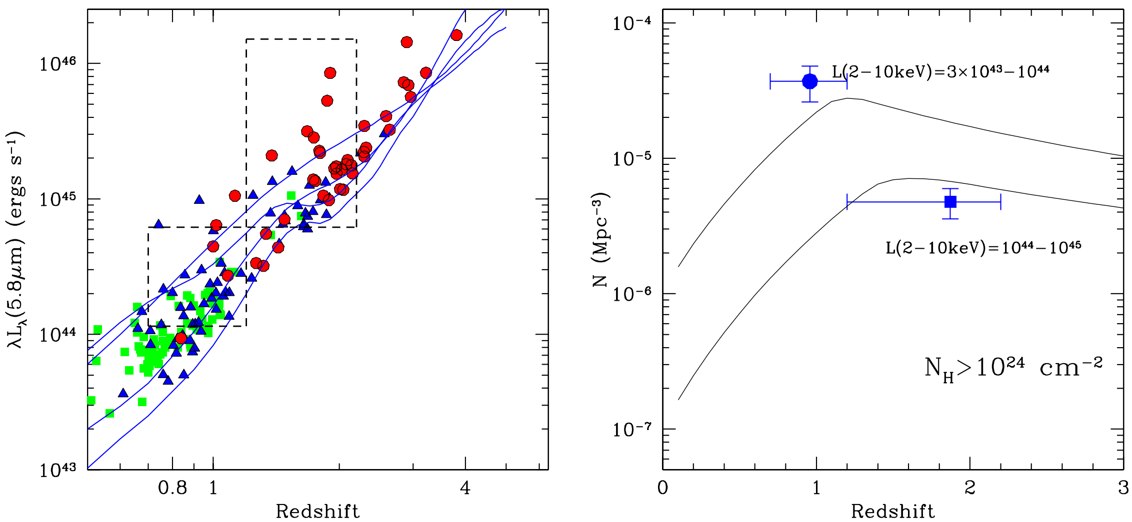

FIG. 8.— [Left panel:] the redshift-luminosity plane of the MIPS sources in cell A (red circles), cell B (blue triangles) and cell C (green squares). Two redshift-luminosity bins chosen for the computation of the CT AGN volume density are marked as dashed boxes. The solid curves show the loci of four SEDs of highly obscured AGN for the 24μm flux limit of 550μJy. [Right panel:] volume density of COSMOS MIPS selected CT AGN. Solid curves are the expectation of the Gilli, Comastri & Hasinger (2007) model in two luminosity bins.

redshift bins. The volume densities of CT AGN and CT QSOs are computed using the sources in Table 7, a 24μm flux limit of 550μJy and correcting the resulting density of MIPS sources for the fraction of CT AGN in Table 4. The densities are reported in Table 8 and in Fig. 8 (right panel). The two L(5.8μm) luminosity bins in Table 8 corresponds to unobscured 2-10 keV luminosities of $3 \times 10^{43} - 10^{44}$ and $10^{44} - 10^{45}$ ergs s^{-1} using the L(5.8μm)-L(2-10 keV) luminosity conversion of eq. 1.

7. DISCUSSION

We analyzed the X-ray properties of a sample of MIPS 24μm sources with a signal to noise ratio > 4 and a 24μm flux limit of $\sim 550\mu$Jy detected in an area of the COSMOS field with deep *Chandra* coverage. 232 of the 919 MIPS sources have a robust *Chandra* detection (Elvis et al. 2008). Additional 47 sources have more than 10 background-subtracted *Chandra* counts within 5 arcsec of the position of the MIPS source, but they are not present in the C-COSMOS and XMM-COSMOS catalogs. These may well be faint X-ray sources just below the adopted detection threshold. The fraction of X-ray detections for the COSMOS bright MIPS sample is therefore between 25% and 30%. $\sim$ 75% of these sources have an X-ray (2-10 keV) luminosity $> 10^{42}$ ergs $^{-1}$, and are therefore likely to host an AGN. For the sources not directly detected in the *Chandra* images we computed stacked count rates in the 0.3-1.5 keV and 1.5-6 keV bands. We found a strong correlation between the hardness ratio of the stacked count rates and the F(24μm)/F(R) flux ratio (and the R-K color). We use the stacked count rates and hardness ratios, together with detailed Monte Carlo simulations, to estimate the fraction of Compton-thick AGN in nine cells defined in the F(24μm)/F(R) − R-K diagram. The simulations were performed assuming that the sources without an X-ray detection are either obscured AGN or star-forming galaxies. The results, reported in Table 4 and Fig. 6, suggest that a large fraction of 'IR excess' sources should host an obscured but active nucleus. In particular, the hard hardness ratios measured in cells A and B, those with the highest F(24μm)/F(R) flux ratio (Fig. 4), would imply a fraction of Compton-thick AGN as high as 0.93–0.73, respectively. These results were obtained by using reasonable assumptions for the AGN and star-forming galaxies X-ray spectra and their normalization to the 5.8μm luminosity. In particular, we adopted for the star-forming galaxies a power law X-ray spectrum with an energy spectral index 0.9, similar to that found in star-forming galaxies accessible to detailed X-ray spectroscopy. To explain the observed hardness ratios without resorting to a large population of CT AGN would require extremely flat or even inverted energy spectral indices for most star-forming galaxies at z=1-2, a spectrum never observed so far in this class of objects at smaller cosmological distances. This would imply a rather extreme cosmological evolution of the X-ray spectrum of star-forming galaxies, that, while cannot be fully excluded, appears nevertheless unlikely. Furthermore, the interpretation of the observed hardness ratio in terms of a high fraction of CT AGN is fully consistent with the results of template fitting to the observed MIPS source's SEDs.

Recently Donley et al. (2008) questioned the 'IR excess' technique to select highly obscured AGN, claiming that CDFS 'IR excess' samples may be more contaminated by moderately obscured AGN and star-forming galaxies than estimated by Daddi et al. (2007) and F08. For the purposes of this paper we limit ourselves to remark that this can hardly be the case for luminous QSOs in cell A. In fact, an unobscured QSO with L(2-10keV)= 10^{44} ergs s^{-1} at z=2.2 (the upper limit of the redshift bin considered in Section 5), would produce between 40 and 80 counts in the C-COSMOS images for the two typical exposure times in Table 2, and it would be easily detected. A QSO with the same redshift and luminosity but with a column density of 5×10^{23} cm^{-2} would still produce between 10 and 20 counts, thus having a high probability of being detected. Should this source be obscured by a column density as high as 10^{24} cm^{-2}

TABLE 8
AGN volume densities

Redshift	$\log(\lambda L_\lambda(5.8\mu m))$ ergs s^{-1}	logL(2-10keV) ergs s^{-1}	CT AGN Mpc^{-3}	Tot. X-ray AGN[a] Mpc^{-3}	Unobscured X-ray AGN[a] Mpc^{-3}
$1.2-2.2$	44.79-46.18	44-45	$(4.8\pm1.1)\times10^{-6}$	1.1×10^{-5}	5.4×10^{-6}
$0.7-1.2$	44.06-44.79	43.477-44	$(3.7\pm1.1)\times10^{-5}$	5.4×10^{-5}	3.0×10^{-5}

[a] evaluated using the La Franca et al. 2005 luminosity function parameterization.

TABLE 9
Previous CT AGN volume densities determinations

Paper	Field	Redshift	Luminosity ergs s^{-1}	CT AGN density
Daddi et al. 2007	CDFS	1.4–2.5	L(2-10keV)=$(1-4)\times10^{43}$	$\approx 2.6\times10^{-4}$ Mpc^{-3}
Fiore et al. 2008	CDFS	1.2–2.6	logL(2-10keV) $\gtrsim 43$	$\sim$ 100% X-ray selected AGN
Donley et al. 2008	CDFS	–	–	54–94%[a] X-ray selected AGN
Alexander et al. 2008	CDFN	2–2.5	logL(2-10keV)=44–45	$0.7-2.5\times10^{-5}$ Mpc^{-3}
Martinez-Sansigre et al. 2007	SWIRE SXDS	1.7–4	$\log L_{bol}\gtrsim 47$	$\gtrsim$ unobscured QSOs
Polletta et al. 2008	SWIRE, NDWFS, FLS	1.3–3	$L(6\mu m)\gtrsim 4\times10^{45}$	37-65%[b] total AGN population
Della Ceca et al. 2008	XMM HBS	0	logL(2-10keV)=43	$(0.8-2.8)\times10^{-5}$ Mpc^{-3}
Della Ceca et al. 2008	XMM HBS	0	logL(2-10keV)=44	$(1-5)\times10^{-7}$ Mpc^{-3}
Della Ceca et al. 2008	XMM HBS	0	logL(2-10keV)=45	$(1-25)\times10^{-10}$ Mpc^{-3}

[a] The lower limit refers to *Spitzer* selection only, the upper limit includes the contribution of AGN selected because their high radio to infrared flux ratio; [b] The lower limit refers to QSO obscured by a compact torus, the upper limit to the global fraction of obscured QSO to the total QSO population in that redshift-luminosity bin.

it would still produce between 6 and 12 counts (direct emission only, without considering the likely contribution from a scattering component), with a non negligible probability of being directly detected. We conclude that unobscured or moderately obscured QSOs cannot be present in the sample of MIPS source without a direct X-ray detection at z=1.2-2.2 and logL(2-10keV)=44–45. This sample may well contain star-forming galaxies. However, if this component is the dominant one, then it would be difficult to explain the high hardness ratio measured for these sources (see above). Similar arguments apply to the sources in the redshift bin 0.7–1.2 and luminosity bin logL(2-10keV)=43.477-44, which are mainly located in cells B and C (see Table 7). We conclude that the 'IR excess' selection appears quite robust, at least regarding AGN with intermediate to high luminosity at z=0.7–2.2.

7.1. *The cosmic evolution of obscured AGN*

The bright flux limit of the COSMOS bright MIPS sample allows a rather limited coverage of the luminosity-redshift plane, see Fig. 8, left panel. Nevertheless, we could select two redshift-luminosity bins in which the 24μm source samples can be considered reasonably complete. This allows us to search for cosmic evolution of obscured AGN, not directly detected in X-rays.

Table 8 gives the volume densities of CT AGN in the two redshift-luminosity bins. They were calculated by correcting the volume density of the MIPS 24μm source for the fraction of obscured AGN not directly detected in X-rays given in Table 4. It should be noted that these densities do not account for CT objects directly detected in X-rays. The identification of a CT spectrum in a faint X-ray source is not a straight-forward task. Previous studies suggest that the fraction of CT AGN in X-ray samples is small, of the order of a few % (Tozzi et al. 2006, Mainieri et al. 2007, Perola et al. 2004), so we do not try to correct our density of CT QSOs for this fraction at this stage.

7.1.1. *The fraction of obscured AGN as a function of their luminosity*

Table 8 also gives the volume densities of X-ray selected AGN in the same redshift bins, computed using the parameterization of the 2-10 keV luminosity function in La Franca et al. (2005). We find that the density of infrared selected, CT QSOs at z-1.2–2.2 is 44% of that of all X-ray selected AGN in the same redshift-luminosity bin ($\sim$ 90% of that of both unobscured and moderately obscured QSOs). Conversely, at z=0.7–1.2 and L(2-10keV)= $3\times10^{43}-10^{44}$ the density of infrared selected, CT AGN is $\sim$ 67% of that of X-ray selected AGN, and 120%, 150% that of unobscured and moderately obscured AGN respectively. This comparison suggests that the fraction of obscured AGN to the total AGN population decreases with the luminosity not only when considering moderately obscured, X-ray selected AGN (Ueda et al. 2003, La Franca et al. 2005), but also including infrared selected, CT AGN.

It is also instructive to compare our estimates to the expectations of AGN synthesis models for the CXB. The expectations of the Gilli et al. (2007) model in the two luminosity bins used in our analysis are plotted in Fig 8. We see that the Gilli et al. model predicts a density of CT QSOs (logL(2-10keV)=44-45) slightly higher than our estimate in the redshift bin 1.2–2.2, but consistent with it at the 90% confidence level. Conversely, the model predicts a density of logL(2-10keV)=43.477–44 AGN at z=0.7–1.2 a factor of $\sim$ 2 lower than our estimates. However, this difference is significant at 1.5σ level. The Gilli et al. (2007) model predicts that the fraction of obscured AGN ($\log N_H > 22$ cm^{-2}, including CT sources) to the total AGN population decreases with luminosity from $\sim$ 75% at Seyfert like luminosities to 45% at QSO luminosities. In summary, our determinations of the CT AGN densities in two luminosity bins agree reasonably well with the Gilli et al. (2007) prediction (Fig. 8). This means again that our findings support the idea that CT AGN follow a luminosity dependence similar to

Compton thin AGN, becoming relatively rarer at high luminosities.

7.1.2. *Comparison with previous studies.*

We compare our estimates of the CT AGN volume density with previous determinations (see Table 9 for a summary).

Several recent papers have been focusing on the search for highly obscured AGN in the CDFS. Using an approach similar to ours, i.e comparison of the ratio of the counts in stacked images in two energy bands with Monte Carlo simulations including both obscured AGN and star-forming galaxies, F08 estimated in the CDFS a density of CT AGN with logL(2-10keV)> 43 and at z=1.2–2.6 similar to that of X-ray selected AGN. This cannot be directly compared with the densities estimated in this paper, because in the same redshift bin we can select only luminous QSOs. However, we note that the F08 estimate is similar to what we find in the C-COSMOS field in the lower redshift bin 0.7–1.2. Daddi et al. (2007), using a somewhat different approach on the same CDFS dataset, estimate that the density of CT AGN is $\sim 2.6 \times 10^{-4}$ Mpc^{-3} at z=1.4–2.5, and infer that their 2-10 keV luminosities are in the range $10^{43} - 4 \times 10^{43}$. The Daddi et al. density is significantly higher than our estimates, and it is $\sim$ 6 times higher than the expectation of the Gilli et al. (2007) model. Donley et al. (2008) recently estimated a conservative lower limit to the *Spitzer*-selected AGN in the CDFS, not directly detected in X-rays. They conclude that the number of AGN with 24μm flux higher than 80μJy is 54-77% larger than for purely X-ray selected AGN. The fraction increases to 71-94% including AGN selected with a high radio to infrared flux ratio. The combined analysis of the COSMOS and CDFS field is clearly needed for a better coverage of the redshift-luminosity plane, and thus to measure the CT AGN luminosity function in several luminosity and redshift bins. This combined analysis will be presented in a forthcoming paper.

Alexander et al. (2008) used again *Chandra* deep fields, but limited their analysis to CT QSOs confirmed through infrared and optical spectroscopy, in addition to X-ray imaging. Using a small sample of four CT QSOs they estimate a density $0.7 - 2.5 \times 10^{-5}$ Mpc^{-3} at z=2–2.5. This is formally higher than our estimate at a similar redshift, but still statistically consistent with it, within their rather large error bars.

Martinez-Sansigre et al. (2005, 2007) and Polletta et al. (2008) looked at highly obscured QSOs of extreme luminosity in the large area SWIRE, NDWFS and FLS surveys (bolometric luminosity $\gtrsim 10^{47}$ ergs s^{-1}). The former authors concluded that their CT QSOs are at least as numerous as unobscured QSOs, a result similar to what we find at slightly lower luminosities in the C-COSMOS field. On the other hand, Polletta et al. (2008) conclude that 37-40% of the QSOs with L(6μm)$\gtrsim 4 \times 10^{45}$ ergs s^{-1} and z=1.3-3 are obscured by a compact torus, while 23-25% are obscured by matter distributed on larger scale. Polletta et al. (2008) do not distinguish between CT and Compton-thin absorbers, however it is reasonable to assume than most objects obscured by a compact torus are CT, and therefore that their fraction is a lower limit to the real CT fraction.

Finally, Della Ceca et al. (2008) estimated the density of CT AGN at three luminosities, by comparing the luminosity function of optically selected, narrow line AGN in the SDSS (Simpson 2005), which must include both CT and Compton-thin AGN, to the luminosity function of X-ray selected Compto-thin AGN, rescaled at z=0 using their best fit evolutionary model. The Della Ceca et al. (2008) densities are listed in Table 9. They agree quite well with the densities estimated in this paper, once they are de-evolved (Della Ceca et al. 2008).

7.2. *Obscured AGN: catching feedback in action*

Our findings indicate that luminous CT absorbers follow the same fundamental correlation with the luminosity found for Compton-thin absorbers. This correlation has been interpreted in the past either in terms of a luminosity dependence of the obscuring "torus" sublimation radius (e.g. Lawrence 1991), or due to the bending of the interstellar gas due to the BH gravitational field (the higher the BH mass the larger the bending, and smaller the fraction of sight lines intercepting the gas, Lamastra et al. 2006). Recently, Menci et al. (2008) introduced a new scenario, in which the absorption properties of an AGN depends both on the orientation to the line of sight and on the time needed to sweep the central regions of galaxy disks. In this scenario the correlation between the fraction of obscured AGN and the luminosity is mainly due to a different timescale over which nuclear feedback is at work. If this is the case, then one may expect that X-ray selected, moderately obscured QSOs are caught at a later stage of feedback activity than highly obscured, CT QSOs. Of course this must be intended on average, because the distribution of the obscuring gas around the nucleus would not be spherically symmetric, and therefore obscuration will depend also on the orientation to the line of sight. As a consequence, some CT QSO seen just along the plane of the obscuring material would be in a similar evolutionary stage as a moderately obscured QSO. A prediction of this evolutionary scenario is that the host galaxies of high luminosity, CT QSOs should be, on average, more star-forming than the host galaxies of unobscured or moderately obscured QSOs of similar luminosity. Interestingly, Stevens et al. (2005) and Page et al. (2004) find that X-ray obscured QSOs have much higher sub-millimeter detection rates than X-ray unobscured QSOs. Alexander et al. (2005) found that most radio identified sub-mm galaxies host X-ray and optically obscured AGN, but that their bolometric luminosity is dominated by star-formation. Martinez-Sansigre et al. (2005, 2008) found little or no Lyman-α emission in a sample of z> 1.7 obscured QSOs, suggesting large scale (kpc) dust distribution. Sajina et al. (2007) and Martinez-Sansigre et al. (2008) report Spitzer IRS spectra dominated by AGN continuum but showing PAHs features in emission in samples of ULIRGs and radio selected obscured QSOs at z$\sim$ 2. Finally, Lacy et al. (2007) find evidence for dust-obscured star formation in the IRS spectra of type-2 QSOs. All these findings are in general agreement with the evolutionary picture.

7.3. *Tests of the AGN/host-galaxy evolutionary scenario*

We were able to select in the C-COSMOS field both unobscured and moderately obscured AGN using direct X-ray detection, and highly obscured, CT AGN selected in the infrared but confirmed through a detailed X-ray stacking analysis. This make our sample ideal to probe the above evolutionary scenario.

Star-formation can be revealed by emission at radio wavelengths (Condon 1992). Radio fluxes, down to a 5σ flux limit of $\sim 65\mu$Jy are available for 43% of the MIPS selected sources. The same fraction of radio fluxes is available for MIPS sources with a direct X-ray detection. Following Schinnerer et al. (2007), the 1.4 GHz luminosity has been computed assuming a spectral energy index of 0.8. Among the 38 sources in cells A and B and in the redshift-luminosity bin z=1.2–2.2 logL(5.8μm)=44.79-46.18 (see Table 7) 18 have a radio detection. Their median logarithmic radio luminosity ($<\log\lambda L_\lambda(1.4GHz)$) is 40.53 ergs s^{-1} with interquartile range 0.18. Putting the radio luminosity of the sources without a radio detection to the limit computed at their redshift reduces the median logarithmic radio luminosity to 40.29 ergs s^{-1} with interquartile 0.18. If the radio luminosity is due to star-formation, it would imply star-formation rates of the order of 300 M$_\odot$ yr^{-1} (e.g. using the correlation given by Condon 1992).

The median logarithmic ratio between the 5.8μm luminosity and the 1.4GHz luminosity of the 38 sources in cells A and B and in the redshift-luminosity bin z=1.2–2.2 logL(5.8μm)=44.79-46.18 (therefore including upper limits on the radio flux) is 4.74 with interquartile 0.12. In the same redshift-luminosity bin there are 25 spectroscopically identified type 1 QSOs in the COSMOS bright MIPS sample, all with X-ray direct detection and eight with a radio flux. Their median radio luminosity (including limits on the radio luminosity) and the median log ratio between the infrared and radio luminosity (including limits on the radio luminosity) are 40.19 and 5.07 respectively. The probability that the luminosity ratio distribution of the 38 sources in cells A and B and the 25 type 1 QSO are drawn from the same distribution is 0.002%, using the F test. This would suggest a slightly stronger radio emission in infrared selected CT QSOs than in unobscured, type 1 QSOs, qualitatively in agreement with our predictions. However, we note that different components, in addition to star-formation, can contribute to the observed radio flux. Furthermore, some residual extinction may still reduce the 8-24μm flux of the CT AGN, which would then underestimate the true 5.8μm rest frame luminosity of these sources. For all these reasons we consider the lower infrared to radio luminosity ratio of CT AGN with respect to type 1 AGN certainly intriguing but not conclusive.

A cleaner test of these predictions can come from infrared spectroscopy of PAH features. Fortunately, the COSMOS infrared selected, CT AGN are bright enough to provide relatively high signal to noise *Spitzer* IRS spectra. These spectra will be able to assess whether nuclear activity and strong star-formation are present at the same time in these object, thus validating or disproving our feedback scenario for AGN obscuration. Finally, if strong star-formation is present in the host galaxies of the CT QSOs, as expected, they should stand out in forthcoming deep Herschel surveys at 70 and 110μm.

8. CONCLUSIONS

We found that 25–30% of the MIPS 24μm sources brighter than 550μJy have a direct X-ray detection down to an X-ray flux limit of a few$\times 10^{-16}$ ergs cm^{-2} s^{-1} . About 75% of these sources are likely to be AGN with L(2-10)keV$> 10^{42}$ ergs s^{-1}. We evaluated the fraction of obscured AGN in the COSMOS MIPS sample without a direct X-ray detection by comparing the count rates and hardness ratio in stacked X-ray images with detailed Monte Carlo simulations. We found that the fraction of AGN in this MIPS sample (both X-ray detected and recovered through their infrared/optical color and a detailed X-ray stacking analysis) is $49 \pm 10\%$. Considering only the sources with z$>$ 0.6 the fraction increases to 0.67 ± 0.06. This is significantly higher than previous estimates obtained using a much shallower X-ray coverage and an analysis of the 24μm-8μm color.

We computed the volume density of the MIPS 24μm selected sources into two luminosity-redshift bins and corrected it for the fraction of CT AGN found in nine cells defined in the F(24μm)/F(R) – R-K diagram, to find the volume density of infrared selected, CT AGN. Our analysis shows that deep X-ray data are the key element to obtain complete unbiased AGN samples, both through direct detection and through dedicated stacking analyses. Of course the latter can provide results on CT AGN valid only in a statistical sense. While the search for and characterization of CT AGN remains one of the main goals of the on-going *Chandra* and *XMM-Newton* ultra-deep surveys of the CDFs (e.g. Comastri & Brusa 2007), the direct X-ray detection of large samples of CT AGN and the accurate measure of their obscuring column densities must await for the next generation of X-ray telescopes with imaging capabilities in the 10-100 keV band, like NuSTAR, NeXT and Simbol-X (Fiore et al. 2008b).

We found that the density of CT QSOs with z=1.2–2.2 and $\log\lambda L_\lambda(5.8\mu m) = 44.79 - 46.18$ and with z=0.7–1.2 and $\log\lambda L_\lambda(5.8\mu m) = 44.06 - 44.79$ are $\sim 44\%$ and $\sim 67\%$ of the density of X-ray selected unobscured and moderately obscured AGN in the same redshift and luminosity bins, respectively.

Our results imply that the correlation between the fraction of obscured AGN with the luminosity found for X-ray selected AGN holds also when considering infrared selected, CT AGNs. If the fraction of obscured AGN is a measure of the timescale over which the nuclear feedback is at work, then unobscured and moderately obscured QSOs should be hosted in more passive galaxies, on average, than those hosting CT QSOs of similar luminosity. Star-formation can be traced at radio wavelengths and we find indeed that the infrared selected CT QSOs at z=1.2–2.2 are more radio luminous (with respect to their 5.8μm luminosity) than unobscured type 1 QSOs of similar redshift and luminosity. Although this result is in line with previous findings we do not consider it as conclusive. Further investigation, as for example direct infrared spectroscopy and far infrared photometry of the candidate CT QSOs, is needed to confirm our evolutionary feedback scenario.

We acknowledge support from ASI/INAF contracts I/023/05/0 and I/024/05/0 and by PRIN/MUR grant 2006-02-5203. FF thanks Mari Polletta for useful comments. The zCOSMOS ESO Large Program Number 175.A-0839 is acknowledged.

REFERENCES

Alexander,D.M., Bauer, F.E., Chapman, S.C. et al. 2005, ApJ, 632, 736
Alexander,D.M., Chary, R.R., Pope, A., Bauer, F.E., Brandt, W.N., Daddi, E., Dickinson, M., Elbaz, D., Reddy, N.A., 2008, ApJ, in press, arXiv:0803.0636
Aussel, H. et al. 2008, ApJin preparation
Bower et al. 2006, MNRAS, 370, 645
Boyle, B.J., Shanks, T., Peterson, B.A. 1988, MNRAS, 235, 935
Brand et al. 2006, ApJ, 644, 143
Brand et al. 2007, ApJ, 663, 204
Brandt, W.N., Hasinger, G. 2005, ARA&A, 43, 1056
Brusa, M., Comastri, A., Daddi, E. et al. 2005 A&A, 432, 69
Brusa, M. et al. 2007, ApJS, 172, 353
Brusa, M. et al. 2008a, ApJ, in preparation
Brusa, M. et al. 2008b, ApJ in press, arXiv:0809.2513
Capak, et al. 2007, ApJS, 172, 99
Civano, F. et al. 2008, ApJ, in preparation
Comastri, A. 2004, in "Supermassive Black Holes in the Distant Universe", Ed. A. J. Barger, Kluwer Academic, vol. 308, p.245
Comastri, A., Gilli, R., Vignali, C., Matt, G. Fiore, F., Iwasawa, K. 2007 Progress of Theoretical Physics Supplement, No. 169, pp. 274-277, arXiv:0704.1253
Comastri, A., & Brusa, M. 2007, proceedings of the conference: "XMM-Newton: the next decade", in press, arXiv:0710.0561
Condon, J.J. 1992, ARA&A, 30, 575
Cowie L.L., Songaila, A., Hu, E.M., Cohen, J.G., 1996, AJ, 112, 839
Cowie L., Barger A., Bautz, M.W., Brandt, W.N., Garnire, G.P. 2003, ApJ, 584, L57
Daddi, E. et al. 2007, ApJ, 670, 173
Della Ceca, R. et al. 2008, A&A, in press, arXiv:0805.1919
Dey, A. et al. 2008, ApJ, in press, arXiv:0801.1860
Di Matteo, T., Springel, V., Hernquist, L. 2005, Nature, 433, 604
Donley, J.L., Rieke, G.H., Perez-Gonzalez, P.G., Barro, G., ApJ, in press, arXiv:0806.4610
Elvis, M. et al. 2008, ApJ, in preparation
Fabian, A.C. 1999 MNRAS, 308, L39
Ferrarese, L. & Merritt, D. 2000, ApJ, 539, L9
Fiore, F., Brusa, M., Cocchia, F. et al. 2003, A&A, 409, 79
Fiore, F., Grazian, A., Santini, P. et al. 2008, ApJ, 672, 94
Fiore, F. et. al. 2008b, Proc. of the workshop "Simbol-X: The hard X-ray universe in focus", Bologna 14-16 May, 2007, MemSAIt, in press, arXiv:0801.0409
Franceschini, A., Hasinger, G., Miyaji, T., Malguori, D. 1999, MNRAS, 310, L5
Gebhardt, K., Kormendy, J., Ho, L. et al. 2000, ApJ, 543, L5
Gilli R., Comastri A., Hasinger G. 2007, A&A, 463, 79
Granato, G.L., Silva, L., Monaco, P., Panuzzo, P., Salucci, P., De Zotti, G., & Danese, L. 2001, MNRAS, 324, 757
Granato, G.L., De Zotti, G., Silva, L., Bressan, A., Danese, L. 2004, ApJ, 600, 580
Hasinger, G., Miyaji, T., Schmidt, M. 2005, A&A, 441, 417
Hasinger, G. et al. 2007, ApJS, 172,
Hasinger, G. 2008, A&Asubmitted
Hopkins, A.M. 2006, ASP Conference Series, V. J. Alonso, H. Ferguson & R. Norris eds. arXiv:0611283
Houck, J.R., et al. 2005, ApJ, 622, L105
Ilbert, O. et al. 2008, ApJ, in press, arXiv:0809.2101
Lacy, M. et al. 2004, ApJS, 154, 166
Lacy, M. et al. 2007, ApJ, 669, L61
La Franca, F., Fiore, F., Comastri A. et al. 2005, ApJ, 635, 864
Lamastra, A., Perola, G.C., Matt, G. 2006, A&A, 449, 551
Lawrence, A. & Elvis, M. 1982, ApJ, 256, L410
Lawrence, A. 1991, MNRAS, 252, 586
Li, Y. et al. 2007, ApJ, 665, 187
Lilly, S.J., Tresse, L., Hammer, F., Crampton, D., Le Fevre, O. 1995, ApJ, 455, 108
Lilly, S. et al. 2007, ApJS, 172, 70
Lutz D. et al. 2004, A&A. 418, 465
Madau, P., Ferguson, H.C., Dickinson, M.E., Giavalisco, M., Steidel, C.C., Fruchter, A. 1996, MNRAS, 283, 1388
Mainieri, V. et al. 2007, ApJS, 172, 368
Maiolino, R. Marconi, A., Salvati, M. et al. 2001, A&A, 365, 37
Maiolino, R., Shemmer, O., Imanishi, M., Netzer, H., Oliva, E., Lutz, D., Sturm, E. 2007, A&A, 468, 979
Marconi, A., Risaliti, G., Gilli, R., Hunt, L. K., Maiolino, R., Salvati, M. 2004, MNRAS, 351, 169
Martinez-Sansigre, A., Rawlings, S., Lacy, M. et al. 2005, Nature, 436, 666
Martinez-Sansigre, A., Rawlings, S., Lacy, M. et al. 2006, MNRAS, 370, 1479
Martinez-Sansigre, A., Rawlings, S., Lacy, M. et al. 2007, MNRAS, 379, L6
Martinez-Sansigre, A. Lacy, M., Sajina, A., Rawlings, S., 2008, ApJ, 674, 676
Merloni, A., Heinz, S. 2008, MNRAS, in press, arXiv:0805.2499
McCracken H. et al 2008, ApJ, in preparation
Menci, N., Fontana, A., Giallongo, E., Grazian, A., Salimbeni, S. 2006 ApJ, 647, 753 632, 49
Menci N., Fiore, F., Puccetti, S. Cavaliere, A. 2008, ApJ, in press, arXiv:0806.4543
Mignoli, M., Pozzetti, L., Comastri, A. et al. 2004, A&A, 418, 827
Page, M.J., Stevens, J.A., Ivison, R.J, Carrera, F.J 2004, ApJ, 611, L85
Pope, A. et al. 2008, ApJin press, arXiv:0808.2816
Perola, G.C. et al. 2004, A&A, 421, 491
Piconcelli, E. et al. 2007, A&A, 473, 85
Piconcelli, E. et al. 2008, in preparation
Polletta, M., Wilkes, B., Siana, B. et al. 2006, ApJ, 642, 673
Polletta, M., Tajer, M., Maraschi, L. et al. 2007, ApJ, 663, 81
Polletta, M., Weedman, D., Honig, S., Lonsdale, C.J., Smith, H.E., Houck, J. 2008, ApJ, 675, 960
Pozzi, F., Vignali, C., Comastri, A. et al. 2007, A&A, 468, 603
Puccetti, S. et al. 2008, ApJ, in preparation
Ranalli, P., Comastri, A., Setti, G. 2003, A&A, 399, 99
Renzini, A. 1996, ARA&A, 44, 141
Salvato M. et al. 2008, ApJ, in press, arXiv:0809.2098
Sajina et al. 2007, ApJ, 664, 713
Silk, J., Rees, M.J. 1998, A&A311, L1
Sanders, D.B. et al. 2007, ApJS, 172, 86
Schmidt, M. 1968, ApJ, 151, 393
Scoville, N. et al. 2007, ApJS, 172, 1
Schinnerer, E. et al. 2007, ApJS, 172, 46
Silva, L., Maiolino, R., Granato G.L. 2004, MNRAS, 355 973
Simpson, C., Rawlings, S., Lacy, M. 1999, MNRAS, 306, 828
Simpson, C. 2005, MNRAS, 360, 565
Steffen, A.T. et al., 2003, ApJL, 563, 23
Steffen, A.T. et al., 2006, AJ, 131, 2826
Steffen, A.T., Brandt, W.N., Alexander, D.M., Gallagher, S.C., Lehmer, B.D. 2007, ApJ, 667, L25
Stevens, J.A. et al. 2005, MNRAS, 360, 610
Tozzi, P. , Gilli R. Mainieri V. et al. 2006, A&A, 451, 457
Treister, E. et al. 2004, ApJ, 616, 123
Treister, E. & Urry, C.M. 2005, ApJ, 630, 115
Treister, E. & Urry, C.M. 2006, ApJ, 652, L79
Trump, J. et al. 2007, ApJS, 172, 383
Trump, J. et al. 2008, in preparation
Ueda, Y. et al. 2003, ApJ, 598, 886
Ueda, Y. et al. 2007, ApJ, 664, L79
Weedman, D.W., Le Floc'h, E., Higdon, S.J.U., Higdon, J.L., Houck, J.R. 2006a ApJ, 638, 613
Weedman, D.W., Soifer, B.T., Hao, L. et al. 2006b, ApJ, 651, 101
Yan, L., Sajina, A., Fadda, D., Choi, P., Armus, L., Helou G., Teplitz, H., Frayer, D., Surace, J. 2007, ApJ, 658, 778